

# Chapter 6

## In-Situ Optical TEM



Peng Wang, Feng Xu, Peng Gao, Songhua Cai, and Xuedong Bai

### 6.1 Introduction

Nanomaterials and devices with diverse response mechanisms to light, including photocatalytic, photoemissive, photoconductive, and photovoltaic effects at the atomic or molecular level, have attracted special attention in recent years [1, 2]. These functional materials play an irreplaceable role in several key fields including pollution disposal [3], clean energy [4], and optoelectronic devices [5].

Transmission electron microscopy (TEM) is one of the most powerful characterization tools for studying nanostructures. In recent decades, the rapid development of aberration correctors has made it possible for conventional TEM to characterize the structure, composition, and spectroscopy of samples at the subatomic scale [6, 7], so as to better understand the principle of material performance, which greatly

---

P. Wang (✉)

National Laboratory of Solid State Microstructures, Jiangsu Key Laboratory of Artificial Functional Materials, College of Engineering and Applied Sciences and Collaborative Innovation Center of Advanced Microstructures, Nanjing University, Nanjing 210093, China  
e-mail: [wangpeng@nju.edu.cn](mailto:wangpeng@nju.edu.cn)

F. Xu

SEU-FEI Nano-Pico Center, Key Laboratory of MEMS of Ministry of Education, Southeast University, Nanjing 210096, China

P. Gao

International Center for Quantum Materials, and Electron Microscopy Laboratory, School of Physics, Peking University, Beijing 100871, China

S. Cai

Department of Applied Physics, The Hong Kong Polytechnic University, Hung Hom, Kowloon, Hong Kong 999077, China

X. Bai

Beijing National Laboratory for Condensed Matter Physics, Institute of Physics, Chinese Academy of Sciences, Beijing 100190, China

promotes the development of nanomaterials [8–11] and devices [12–15]. However, this characterization only observes the static states of materials, that is, obtaining *ex situ* information. With the rising experimental requirements of advanced optical functional materials and devices, it is of great importance to introduce illumination into the TEM to realize *in situ* measurements for the determination of correlations between optical properties and microstructures [16].

Due to the confined geometry inside the TEM chamber, early research usually introduced the light stimuli generated by the external light source into the microscope through light-paths composed of optical fibers and mirrors. The first reported *in situ* illumination TEM experiment was carried out over three decades ago by K. Suzuki et al. [17]. They managed to insert an optical fiber into the specimen chamber and studied the dislocation motion in IIB-VIB compounds with direct illumination. From then on, several groups upgraded the TEM column for modification. Y. Ohno et al. designed an opto-TEM system by fixing mirrors and optical fibers into the JEOL JEM 2000-EX microscope to obtain TEM data, photoluminescence (PL), and cathodoluminescence (CL) spectra simultaneously [18–21]. M. Picher et al. replaced the objective aperture holder with a rod-mirror assembly to deliver the laser and collect CL and Raman spectroscopic signals [22]. B. K. Miller et al. developed an optical fiber system for *in situ* ultraviolet (UV)-visible illumination to study nanostructured photocatalysts [23]. Apart from direct modifications to the TEM column, customizing versatile TEM holders are also considered low risk, easy ways to introduce light-paths into the TEM. Tanabe et al. developed a new type of TEM holder for collecting CL light [24]. D. Shindo et al. developed an opto-TEM holder with a laser irradiation port combined with a piezo-driven probe [25]. F. Cavalca et al. developed both a lens-based and a fiber-based opto-TEM holder [26]. Gatan Inc. eventually developed this method into the commercial Gatan sample holders.

The major advantage of introducing external light stimulus through the light-path is broadband and reversibility. A light-path can introduce illumination from several external light sources and collect optical signals emitted from the sample simultaneously, which enables the detection of PL, CL, and other spectra. Besides, lenses in a light-path have high power transmission efficiency, as well as the capability of focusing light to produce a tiny probe with high intensity [26].

Although the introduction of *in situ* illumination can be achieved by the light-path method, the complex optical connection, and large-scale modifications of TEM and holders may lead to a decrease in reliability and general use. In addition, it is difficult to carry out a joint test of various *in situ* methods, such as electrical and mechanical, in the micro-region of the sample due to the occupation of the space by the light-path components. This problem can be solved by the method based on TEM-STM holders. P. Gao et al. first employed a light-emitting diode (LED) chip inside the *in situ* TEM-STM holder to determine the photoconducting response on the bending of ZnO nanowires [27]. The same setup was then used by S. Yang et al. to study the coupling of the piezoelectric effect and the electrical, optoelectronic, and electromechanical properties of ZnO nanowires [28]. Later, H. Dong et al. upgraded their setup with simultaneous picoampere precision and high stability for atomic resolution imaging [29]. They managed to build a single nanowire quantum dot

heterojunction solar cell (QDHSC) on the holder and achieve a nearly ideal quantum efficiency via precise interfacial tuning [30].

While the TEM-scanning tunneling microscope (STM) holder provides a superior platform for multi-functional in situ micro-area testing, the stability and miniaturization of modification can be further improved by the solution based on in situ microelectromechanical system (MEMS) chips. Due to the recent development of MEMS technology, increasing functional devices can be integrated into a micro-chip to build a lab-on-chip, which makes it a hot spot to apply in situ MEMS chips instead of traditional devices for in situ research [31–33]. Under the reference of mature and widely used commercial products, S. Cai et al. provided a practicable method to realize in situ optoelectrical experiments by designing a MEMS chip with a LED mounted on it [34]. Unlike traditional large size light sources such as lamps and lasers, LEDs with smaller sizes are appropriate for in situ illumination in the front of the TEM holders, thus minimizing modifications to the in situ TEM holders.

These different technical solutions all have preponderant applications in specific material systems and research interests. For the best experimental results, a careful selection of techniques and facilities is important. Different from some existing reviews of in situ optical fields [35], in order to let readers better understand the implementation details and application fields of different technical routes, in the next session, we will first describe the implementation details of the three major technical routes in detail. In the third section, we will describe three typical application fields of photocatalysis, PL/CL, and photocurrent according to different application fields. Finally, we will look into the future of in situ opto-TEM technology in the fourth section.

## 6.2 Three Typical Technical Routes for in Situ Optical Experimental Setups

### 6.2.1 Based on Light-Path

Techniques based on mirrors and/or fibers inside a TEM chamber for illumination and detection are summarized below. Mirrors fixed inside a TEM chamber can be used to collect and focus the emitted light from the specimen. With the combination of optical fibers, mirrors, and optical lens, the light-path designed for meeting specific research demands can be achieved with a broadband of light sources and reversible path.

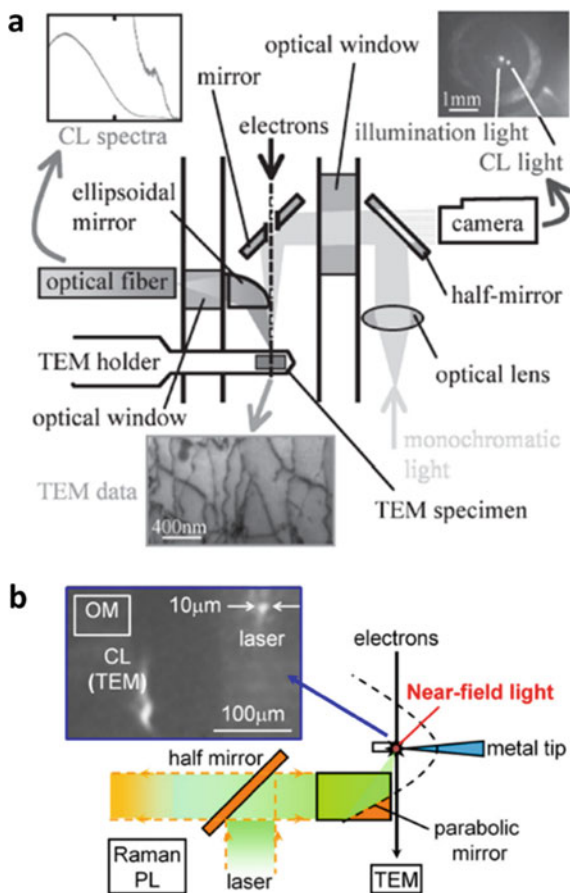
#### Methods

The in situ opto-TEM observation apparatus developed by Y. Ohno et al. combined mirrors and an optical lens to introduce a monochromatic light onto the specimen in the TEM [19]. As shown in Fig. 6.1a, the monochromatic light beam was first collimated by an optical lens outside the TEM. Then, the light beam was reflected by

a half mirror and introduced into the TEM through an optical window attached on the side of the TEM column. It was reflected to the sample by a reflection mirror in the column, which was located above the objective lens and on the axis of an electron beam. The reflection mirror just below the electron source had a small opening to pass through the electron beam. The horizontal displacement of the optical lens would change the position of the light spot on the specimen surface, which is on the order of  $100\ \mu\text{m}$  diameter. For collecting luminescent light from the sample, an ellipsoidal mirror was inserted inside the gap of the pole pieces of the objective lens to focus the emitted PL and CL light to an optical fiber. The optical fiber then transmits the light into a monochromator.

Y. Ohno et al. further improved the system to reach a smaller sized light probe with a near-field light (shown in Fig. 6.1b) [21]. In this apparatus, the laser beam from an optical fiber was first paralleled with the optical lens and then introduced into the microscope by a half mirror. The introduced light was parallel to the revolution axis of the parabolic mirror and could be converged on the focus of it. Most of the

**Fig. 6.1** Schematic view of an in situ opto-TEM apparatus for **a** illumination, and **b** micro- and near-field photo-excitation. An image of the CL signal and a laser spot is shown in the inset of **b** (a Reproduced with permission from Ref. [19], Copyright 2009, John Wiley and Sons; b reproduced with permission from Ref. [21], Copyright 2014, Elsevier)

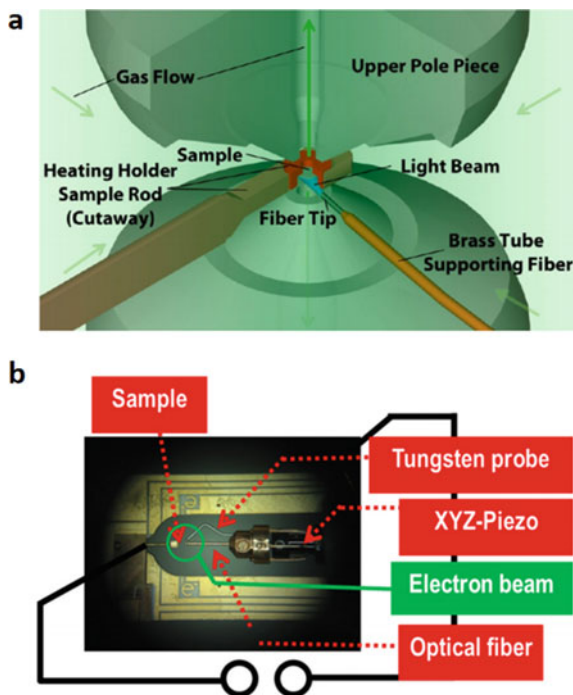


laser light was transmitted to the focus, forming an intense far-field light probe of  $10\ \mu\text{m}$  in diameter. A  $514.5\ \text{nm}$  laser light was used to illuminate the tip and the power density was on the order of  $2 \times 10^3\ \text{W/m}^2$ . A tungsten tip was then fixed close to the specimen for the purpose of the near-field light. Due to the tip-enhanced effect, a near-field light was induced adjacent to the tip. In this case, the path of the emitted light was identical to that of the introduced light.

The apparatus improved by Y. Ohno et al. could achieve a smaller beam spot and near-field light excitation. Nevertheless, the achievable functions by these means are still relatively limited. To realize the characterization of multiple materials and phenomena, P. Crozier et al. designed an opto-environmental transmission electron microscope (ETEM) setup for UV-visible illumination of specimens in photocatalytic experiments (Fig. 6.2a) [36]. The optical fiber fixed inside a brass tube could provide light illumination, and the fiber tip could lead the light onto the specimen. Besides, a piezo-driven optical holder which contains a multimode fiber to provide illumination could attain greater flexibility and microzone illumination (Fig. 6.2b) [37]. On this basis, Gatan developed commercial sample holders with more functions by combining fibers and mirrors into holders.

Figure 6.3a shows a Gatan Vulcan™ CL detector which consists of a sample holder with the sample elliptical aluminium mirrors that are positioned above and below the specimen. The emitted light could be converged by the collecting mirrors into the optical fibers and then directed into the detector [38]. Although the light signal

**Fig. 6.2** Schematic view of **a** an opto-ETEM apparatus (reproduced with permission from Ref. [36], Copyright 2013, American Chemical Society) and **b** a piezo-driven optical holder (reproduced with permission from Ref. [37], Copyright 2015, IOP Publishing)



emitted from the specimen under illumination could be gathered from anywhere as a result of the fixation of collecting mirrors above and below the specimen, the most efficient region for collection is the focal point with a size of  $\sim 100 \mu\text{m}^2$  of the collecting mirrors. The range of dispersion of this Gatan Vulcan™ CL detector is from 5 to 30 meV. Figure 6.3b shows a cryo-CL holder in ETEM designed by M. Vadai et al. and Gatan, Inc. [39]. The parabolic mirrors are able to focus the light and the electron beam can pass the wide aperture with  $500 \mu\text{m}$  in diameter of the adjacent mirrors above the sample. The temperature could be precisely controlled with an error of  $\pm 0.1$  K. Compared to the modifications to the TEM chamber, the holder integrated with mirrors and fibers is more flexible, adaptable, positionally accurate, and sharable for different TEMs.

### Functions

The functions based on the method of light-path are broadband light and reversibility of the optical path.

First, optical fibers, as a kind of flexible light source, can provide control of light illumination through connecting to laser diodes with different wavelengths of light, which is a distinct advantage in contrast to the light source with a single wavelength (Fig. 6.4a) [37].

Secondly, for the method developed by Y. Ohno et al., the laser light from an optical fiber was directed into the TEM column by a half mirror. Then, PL, CL, and Raman signals generated by the laser beam could be gathered by the parabolic mirror. Via the same light-path, these emitted lights were collimated into parallel lights, exported into a 140 mm spectrometer, and finally collected by a CCD detector (Fig. 6.4b) [20]. Thus, the path of introduced light is the same as that of emitted light. By means of this method, the optical spectra data and the TEM data could be obtained simultaneously, and the optical properties of an extended defect could be analyzed with a typical spatial resolution of about 200 nm and a spectral resolution about 1 meV in the spectral range of 1.9–3.3 eV [19]. Besides, the modified in situ opto-TEM observation apparatus is applicable for in situ photo-excitation measurements (Fig. 6.5) [21]. Far-field collimated light transmitted into the TEM can form an

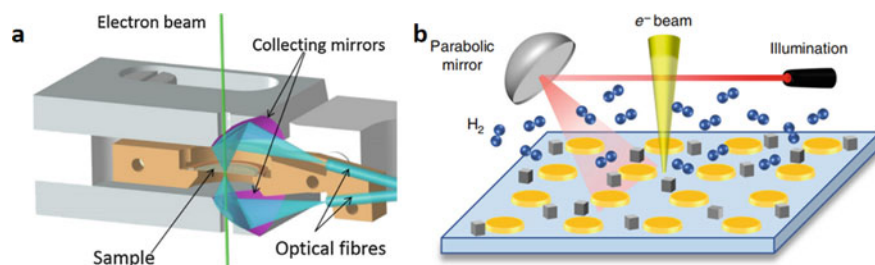


**Fig. 6.3** The schematic view of **a** a Gatan Vulcan™ CL detector (reproduced with permission from Ref. [38], Copyright 2017, Elsevier) and **b** a cryo-CL holder in ETEM (reproduced with permission from Ref. [39], Copyright 2018, Springer Nature)

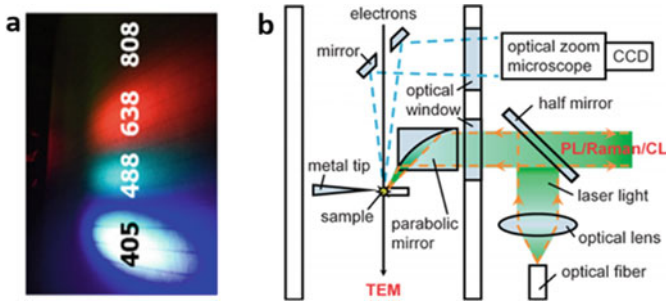
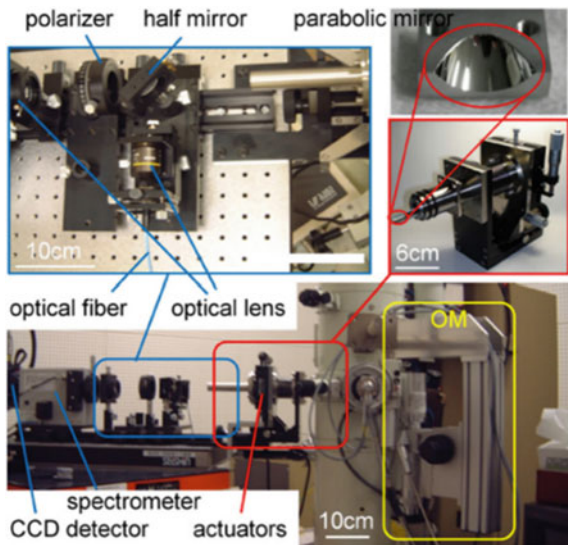


**Fig. 6.4** The schematic view of **a** optical fibers connected to different laser diodes (reproduced with permission from Ref. [37], Copyright 2015, IOP Publishing) and **b** an in situ opto-TEM apparatus (reproduced with permission from Ref. [20], Copyright 2012, The Japan Society of Applied Physics)

intense light probe of 10  $\mu\text{m}$  in diameter, which induces an intense near-field light adjacent to the metal tip apex.

Meanwhile, light illumination and optical detection could be achieved by inserting optical fibers into a sample holder. The Gatan CL holder, which was developed by this method, could achieve CL detection for STEM samples. The mirrors around the sample can collect the emitted light signal, which was simultaneously induced by the electron beam [38], and achieve a reversible light-path. Also, the emitted light signal from the specimen could be collected from anywhere in the sample disk, and thus highly efficient collection could be accomplished.

**Fig. 6.5** An external view of an in situ opto-TEM apparatus for micro- and near-field photo-excitation (reproduced with permission from Ref. [21], Copyright 2014, Elsevier)



## 6.2.2 Based on the TEM-STM Holder

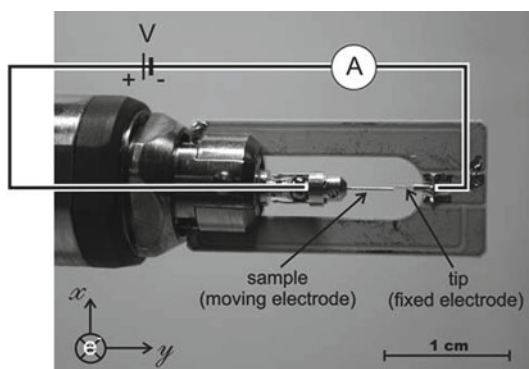
As shown in Sect. 6.2.1, the techniques based on mirrors and/or fibers inside a TEM chamber for illumination and detection have an obvious limitation on the capabilities of in situ electrical and mechanical TEM observation. However, the high-performance TEM-STM sample holder is shown in Fig. 6.6, which allows the direct visualization of the operation of nanoscale devices mounted on it, and can be employed to elucidate the charge transfer and microstructural evolution during the operation of lithium-ion batteries [40] and resistive memories [41, 42] and study the liquid-like deformation mechanism of sub-10-nm crystalline silver particles [43]. As electronic packaging technology develops, the common surface-mounted LED is nearly  $3 \times 1.5 \times 0.5$  mm in size. Besides, TEM-STM holders have electrodes with moderate distances fabricated on the sample side, which can provide voltage for LED lighting. Furthermore, considering that the piezo-part takes up most of the space in TEM-STM holders brings complexities on methods of using lens and fibers, thus using LEDs as light sources has more simplicity and better air tightness for no reformation on the TEM. By combining the LEDs with the TEM-STM holders, in situ optoelectrical studies of these energy devices can offer valuable insights on the fundamental understanding of the critical factors for further enhancing device performances.

### Methods

P. Gao et al. reported electrical transport coupled with optical and piezoelectric properties of individual ZnO nanowires by introducing ultraviolet illumination during TEM imaging, which can be recognized as a typical case of combining LED with TEM-STM holder [27]. The experimental setup is designed as schematically shown in Fig. 6.7.

Based on that, H. Dong et al. developed an in situ photoelectric system shown in Fig. 6.8, which combines a custom-designed photoelectric TEM holder reformed on a commercially available Nanofactory TEM-STM holder with an external electric measurement system [29, 30]. As shown, the homemade in situ photoelectric setup

**Fig. 6.6** Schematic diagram of one kind of TEM-STM sample holder (reproduced with permission from Ref. [44], Copyright 2007, Springer Nature)



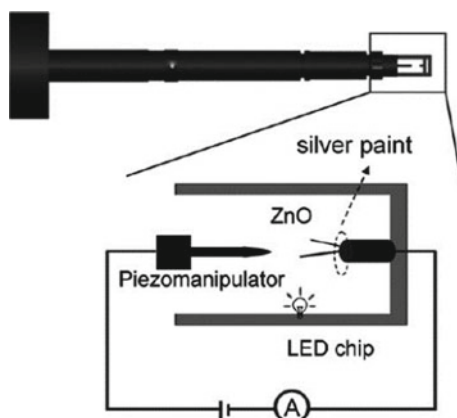


**Fig. 6.7** Setup for in situ TEM photoelectric measurements (reproduced with permission from Ref. [27], Copyright 2009, Royal Society of Chemistry)

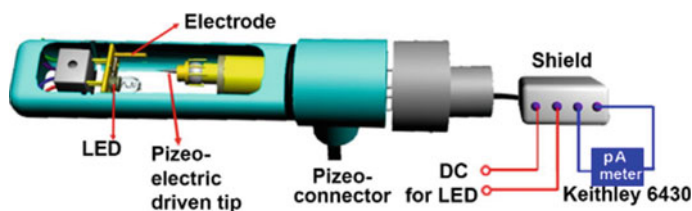


**Fig. 6.8** Schematic diagram of the in-house-designed photoelectric sample holder (reproduced with permission from Ref. [29], Copyright 2018, Royal Society of Chemistry)

replaces the original electrical measuring system, which was previously inserted into the slot of the TEM-STM holder. Besides, the shielding system connected with a picoampere meter is designed to measure ultra-small currents.

Sapphire ( $\text{Al}_2\text{O}_3$ ) was selected as the substrate and serves as a support for both the LED and electrode. Due to its high resistivity ( $>10^{11} \Omega\cdot\text{cm}$ ), the sapphire support can reduce current interference during imaging. The preparation procedure of the photoelectric measurement system is shown in Fig. 6.9. First, the sapphire substrate is cut into pieces of size  $4.0 \times 2.4 \text{ mm}$ . Small holes with diameter of 0.3 mm are then drilled to affix the Cu grid. Next, an appropriately sized shadow mask was placed on the sapphire substrate; after which, a gold film was deposited by planar magnetron sputtering to make the selected area conductive. Subsequently, the LED is placed on the substrate using conductive silver adhesives. Finally, the LED is activated to emit light using the indigenous power system.

By implanting different kinds of LEDs on the sapphire substrate, lights of different wavelengths can be emitted inside the TEM as Fig. 6.10 depicts. In addition, different LEDs can be simultaneously implanted on the holder and the intensity of the light

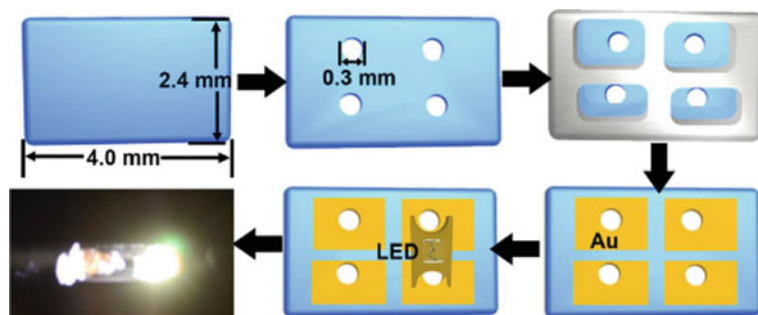


**Fig. 6.9** Preparation of the photoelectric block and a photograph of the lighted LED emitting white light (reproduced with permission from Ref. [29], Copyright 2018, Royal Society of Chemistry)

can be controlled by adjusting the output voltage of the homemade power supply system (Fig. 6.11).

The quality of the TEM image was deteriorated when using the DC-regulated power supply or the battery, originates from the unstable output voltage. To circumvent this problem, a stable DC output voltage system was designed and composed

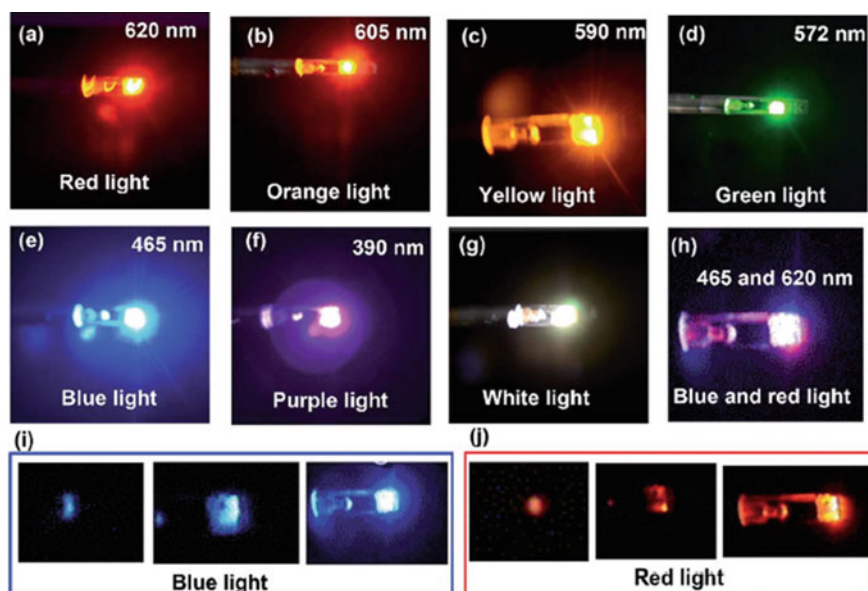
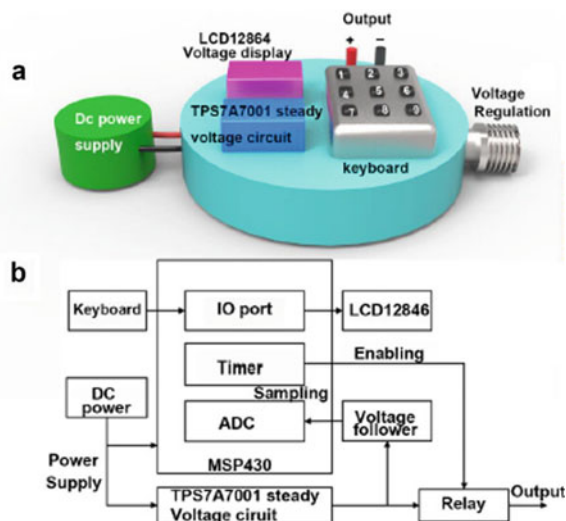


**Fig. 6.10** Visible light emission of different wavelengths from LEDs implanted on the holder inside the TEM. **a–g** show red, orange, yellow, green, blue, purple, and white emissions, respectively. **h** Both red and blue light can be switched on simultaneously. The intensity adjustment of blue (i) and red light (j). (reproduced with permission from Ref. [29], Copyright 2018, Royal Society of Chemistry)

**Fig. 6.11** **a** Schematic diagram of our power supply for the LED. The precision of the voltage controller can be increased to measure voltages of 0.01 V. **b** System layout diagram (reproduced with permission from Ref. [29], Copyright 2018, Royal Society of Chemistry)



of five parts: a commercial DC power supply that functioned as the power source, an ultra-low-dropout chip TPS7A7001 for steady voltage, a keyboard for voltage output time setting, an LCD12864 display module to display the voltage values, and a regulator to adjust the voltage as displayed in Fig. 6.11a. The working principle of this system is demonstrated in Fig. 6.11b. This design allows for an ultrahigh steady voltage output of a certain magnitude while converting commercial direct current into ultra-steady direct current output. Thus, high-resolution and stable TEM images at atomic level can be achieved when irradiated by light from the LED. Besides, it is worth noting that when LED being switched on and off, it would induce significant drift which would break the contact of tip onto the sample. Therefore, the actual operating procedures should follow the sequential steps: TEM imaging—LED on—waiting for stabilization—contact tip—close column valves—electrical measurement.

## Functions

It is worth noting that by precisely controlling the movement of the Pt tip of the TEM-STM holder, the custom-designed photoelectric TEM holder can achieve in situ dynamic observation under multiple stimuli, such as stress and voltage load. In combination with the LED fixed on the TEM-STM holder, P. Gao et al. investigated the piezoelectric effects of ZnO nanowires under UV illumination [27]. As shown in Fig. 6.12, with increased bending of ZnO nanowire by applying stress, the photocurrent shows an obviously decreasing trend at a bias of 5 V. After turning off the LED, the photocurrent undergoes a decay time which shortens with increased bending [27]. This example clearly displays the typical functions of the photoelectric system.

The accuracy of a photocurrent measurement can be further improved when adding a designed shielding system in the circuit [27]. The detail of the shielding

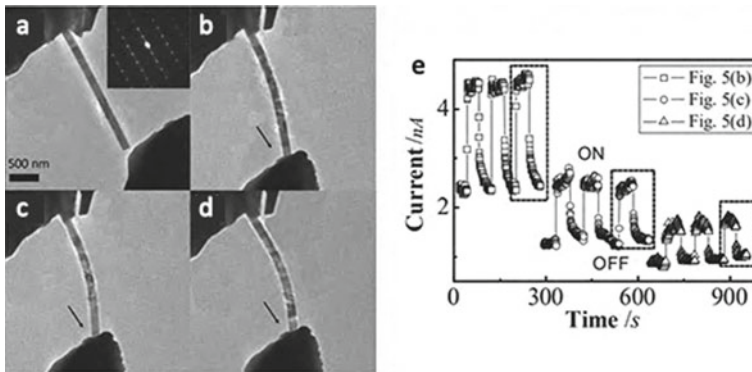


**Fig. 6.12** **a** TEM image of the initial ZnO nanowire. **b–d** TEM images of bending ZnO nanowire. **e** Corresponding photocurrent and dark current and response of the ZnO nanowire for three different bending cases (reproduced with permission from Ref. [27], Copyright 2009, Royal Society of Chemistry)

system is shown in Fig. 6.13a. In the Keithley Model 6430 Sub-Femtoamp Remote SourceMeter, the triax connector includes a central conductor with a connector (High), an outer shell (Low) for electrical measurement, and an inner shell (Guard) of DC shielding to reduce noise in the measurement. In the DC shielding, the guard port is connected to the inner port to enable its potential as the same as the high port and prevent current leakage from the sample. External electrostatic shielding is to eliminate the influence of ambient electric and magnetic fields. As depicted in Fig. 6.13b, after multiple measurements and while the LED is being switched on and off, the shielding system can achieve a current test accuracy within 0.5 pA. Thus, the designed shielding system is suitable for measuring ultra-small current and providing a method for precise explaining the relationship between crystal structure and device performance.

### 6.2.3 Based on in Situ MEMS Chips

While the application of in situ TEM-STM holders provides an efficient method for in situ experiments, the mechanical contact between movable tips and samples often leads to stability reductions, which can hardly meet the requirements of high-resolution in situ characterization.

With the recent developments of MEMS technology, the combination of an in situ holder and specially functionalized MEMS chips has been recognized as a superior route for performing in situ investigations. The MEMS chip serves as a functional sample carrier that can provide localized physical or chemical stimuli for in situ measurements without modification of the TEM or holder. The functional devices on the chips are micro- or even nanoscale, which can be directly set at the position

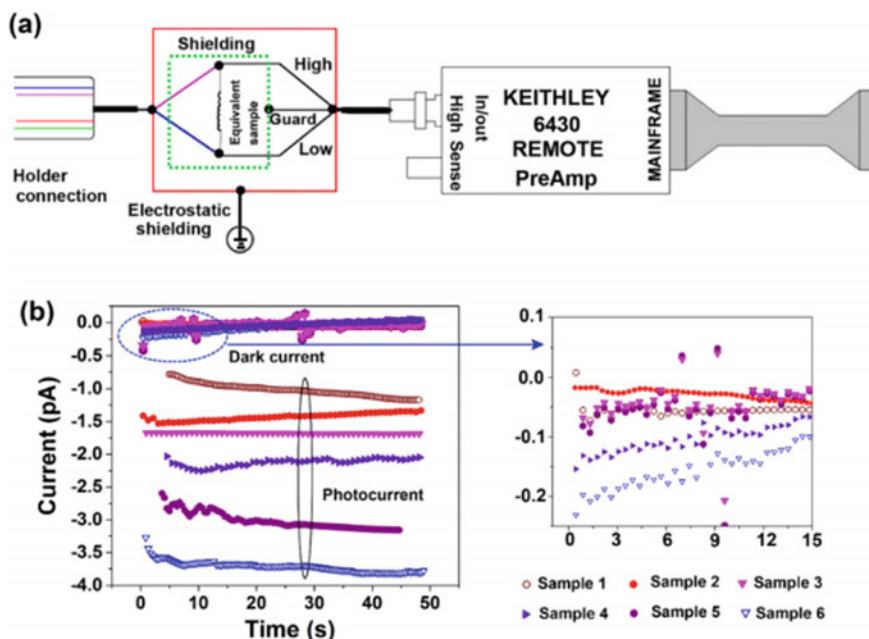


**Fig. 6.13** **a** Schematic of the shielding system in current measurement. **b** Current–time curves in the dark and under light exposure (reproduced with permission from Ref. [29], Copyright 2018, Royal Society of Chemistry)

of the sample and thus accurately apply various stimuli to the micro-area where the samples located.

With the advantages such as high working efficiency, high sample stability, and easy operation, a variety of in situ MEMS chips used in thermal [45], electrical [32, 46], mechanical [32], and liquid/gas environmental [47] in situ tests have been developed; however, MEMS chips with photoelectric functions have not attracted widespread attention. Through a combination of an LED and MEMS chip, not only highly stable in situ illumination conditions can be achieved, but also the joint in situ testing of various environmental conditions and device conditions can be expanded in the future. In addition, the light components on the MEMS chips can be further upgraded to micro-fibers, lenses, or even laser diodes.

## Method

Figure 6.14 is a schematic diagram of the optoelectrical MEMS chip developed by S. Cai et al. [34]. This optoelectrical MEMS chip is specially designed to adapt commercialized in situ TEM heating systems, which usually consist of a controlling computer, power supply, TEM holder, and heating chips. Typical products such as DENS solution DH30 [48] or Protochips Thermal E-chips [49] usually have four needles (Fig. 6.14c) for electrical connection with MEMS chips, which can be adapted for optical and electrical functions.

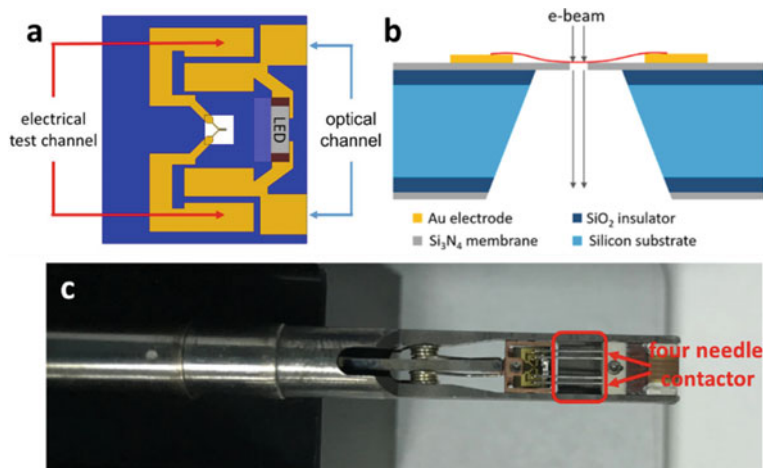


**Fig. 6.14** **a** Plane-view and **b** cross-sectional structure of an in situ MEMS chip. The yellow area represents the four gold electrodes on the chip surface, and the LED is connected to the middle two electrodes, facing the sample area. The outer two electrodes are connected to two micro-electrodes in the sample area. **c** Top views of the tip of the DENS solution DH30 holder, showing the four needle contactors for electrical connections (reproduced with permission from Ref. [34], Copyright 2018, Elsevier)

As shown in Fig. 6.14a, gold electrodes deposited on the chip surface serve as electrical and optical channels. The outer two electrodes are connected to two micro-electrodes in the centers of the chips, where a window is opened for passing through the electron beam and covered by the suspending  $\text{Si}_3\text{N}_4$  membrane with tiny holes to support the transferred samples. For low-dimensional samples such as nanowires and 2D materials, it is possible to directly transfer them onto the micro-electrodes, whereas cross-sectional samples prefer deposited Pt welding for electrical connections using focused ion beam (FIB) systems.

The side-emission LED is connected to the middle two electrodes, facing the sample area to provide in situ illumination. Appropriate LEDs should meet these requirements: (i) the compatibility of the holder with an additional LED chip, (ii) direct light illumination over the sample area, and (iii) no magnetic components to avoid imaging distortion. By adopting the proper commercial LEDs with different wavelengths as shown in Fig. 6.15, this in situ MEMS chip can produce a variety of in situ illumination conditions inside the TEM chamber.

To utilize both electrical and optical channels for illumination control and high accuracy detection of the electrical signal from the sample, a Keithley dual-channel source measure unit (SMU) was used as the power supply and signal detector. A user-friendly custom control system was programmed in LabVIEW software to achieve remote control of this MEMS-chip-based in situ optical system. The interface of the control program is shown in Fig. 6.16. With basic functions such as changing working modes, adjusting working parameters, presetting input waveforms, and showing I/O

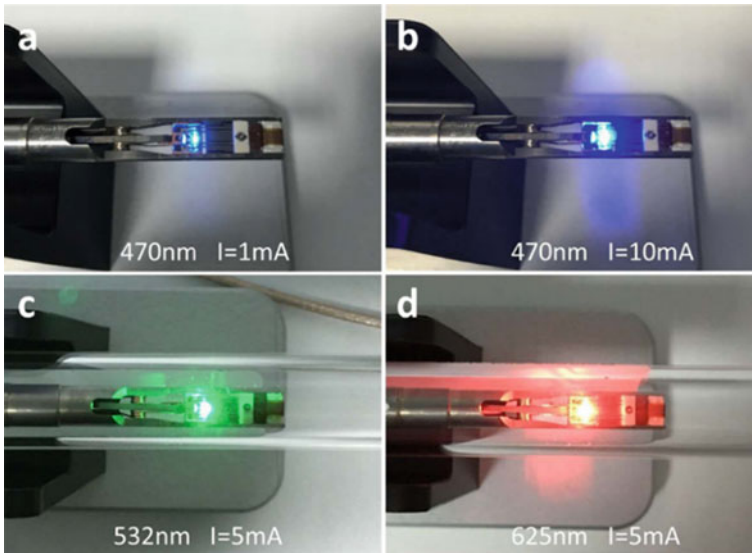


**Fig. 6.15** Commercial LEDs with different wavelengths are implanted on the in situ MEMS chips and operate under real working conditions (reproduced with permission from Ref. [34], Copyright 2018, Elsevier)

status, one can freely adjust the light intensity and obtain electrical data automatically, with all signal curves displayed in real time.

### Functions

The use of the in situ optoelectrical MEMS-chip-based system ensures that in situ illumination can be simultaneously applied with electrical measurements to the sample inside the TEM chamber with minimum modifications. This in situ system can achieve a variety of lighting conditions with the selection of commercial LEDs with different wavelengths. In addition, its favorable stability under working conditions makes it possible to be combined with advanced TEM techniques such as aberration-corrected S/TEM, electron energy loss spectroscopy (EELS), and energy dispersive spectroscopy (EDS) to achieve atomically resolved in situ observation and spectroscopic measurements.

The intensity of light illumination can be quantified by numerical simulation. This simulation was carried out based on an accurate optical model of the entire sample system. The maximum incident light intensity in the sample area reaches  $150 \text{ W/m}^2$  under a forward current of 5 mA for the blue LED (470-nm working wavelength), which can be accurately adjusted by controlling the input current. The electrical Joule heating generated by circuits may lead to decreased sample stability. However, this thermal drift quickly reaches a steady state within approximately 2 min. As shown in Fig. 6.17, the drifting test using an FIB-prepared cross-sectional sample with the LED in a working state suggests that the drifting rate soon decreased to less than 1 nm/min

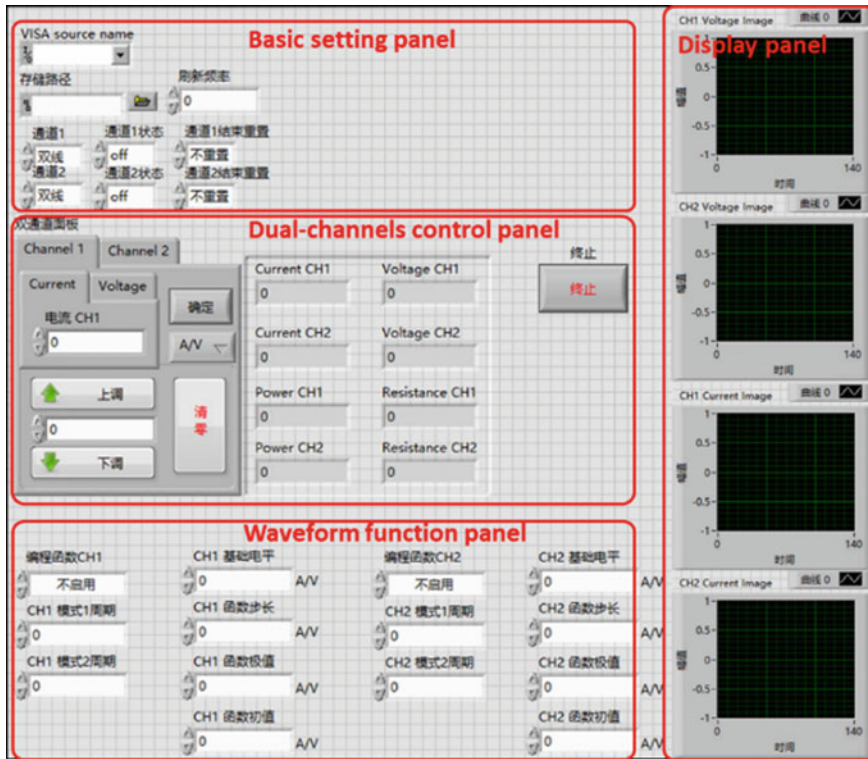
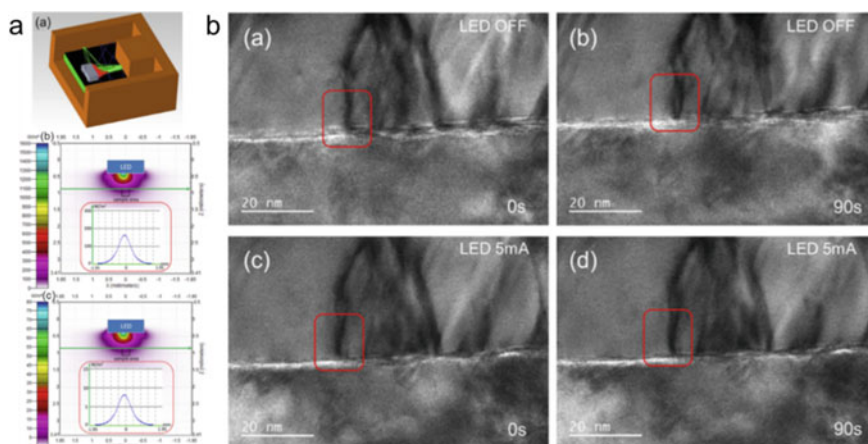


Fig. 6.16 The control interface of an in situ optoelectrical system programmed with LabVIEW

after reaching a steady state. This level of stability meets the requirements for atomic resolution HRTEM and HRSTEM imaging, as well as spectroscopic analyses such as EDS and EELS.

### 6.3 Applications

Since the first in situ opto-TEM work from 1984, this technique has already gone through several generations with the development of both in situ facilities and TEM hardware. From modification of the TEM chamber to specified in situ holders and MEMS chips, in situ optical measurements have become more available and user friendly. However, the combination with new types of TEMs like ETEMs has effectively extended the characterization range and understanding of functional materials working for pollutant disposal, semiconductors, and clean energy. For typical research contents focused on different physical mechanisms, such as photocatalysis,



**Fig. 6.17 Quantification of light intensity and evaluation of sample drifting rate.** **a** Simulation result of light intensity distribution, the maximum incident power density at sample region is  $150 \text{ W/m}^2$ . **b** TEM images taken with the LED off and on at 0 s and after 90 s, respectively. The sample drift rate was less than  $1 \text{ nm/min}$ , suggesting that any additional thermal drift induced by the LED illumination to the sample was small (reproduced with permission from Ref. [34], Copyright 2018, Elsevier)

PL/CL, and photocurrents, in situ illumination/analysis of photosignals plays an irreplaceable role for structure–property exploration. Also different in situ optical techniques have respective application advantages, and the selection should be based on the sample status and photoresponse properties to be studied. Three application topics for in situ optical measurements on physical mechanisms of photocatalysts, PL/CL, and photocurrents will be reviewed in this section, which may provide available references for researchers to design and conduct in situ optical experiments.

### 6.3.1 Photocatalyst

Due to diminishing fossil fuel reserves, a promising solution that generates clean carbon energy from renewable resources, such as sunlight, has attracted much attention [50]. However, the petrochemical industry and fuel consumption have induced serious atmospheric pollution, which also makes pollutant disposal a critical task. Photocatalysts provide a possible solution for the recombination of chemical bonds in a much simpler way, which may be widely used in the future environmental protection industry [3]. For further understanding of underlying fundamental reaction mechanisms and structure–property relationships of photocatalysts, it is necessary to characterize their behaviors under real working conditions using in situ investigations.

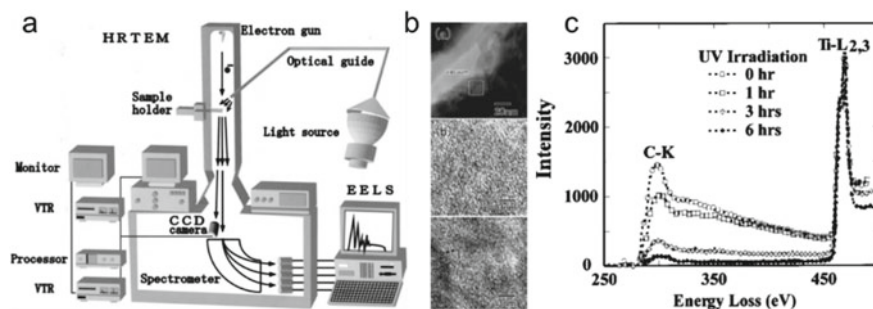


**Fig. 6.18** **a** Schematic diagram of an in situ TEM observation system for photochemical reaction. Ultraviolet light is introduced into a 200 kV high-resolution electron microscope through an optical guide. **b** Electron micrograph of a hydrocarbon/TiO<sub>2</sub> sample which had been illuminated for 3 h. **c** EELS spectra with ultraviolet irradiation. The peak of the carbon-K edge, which shows the existence of organic materials, has decreased with increasing ultraviolet irradiation (reproduced with permission from Ref. [51], Copyright 2004, AIP Publishing)

K. Yoshida et al. constructed an in situ TEM system which introduced optical guides directly into the TEM chamber for observation of the photoreactions (Fig. 6.18a) [51]. This system can provide a light intensity up to 10 mW/cm<sup>2</sup> at a sample plane with a light wavelength of 360 nm, applicable for stimulating photocatalytic reactions of hydrocarbons on TiO<sub>2</sub> films. HRTEM images reveal a clearer lattice structure of TiO<sub>2</sub> after irradiation than before (Fig. 6.18b), which suggests a decomposition of the organic material covered on TiO<sub>2</sub>. An EELS spectrum also shows an obvious decrease of carbon-K edge ( $E = 283.8$  eV) occurring after long time UV irradiation, further demonstrating the photocatalyzed organic decomposition phenomenon (Fig. 6.18c). Further studies on oxygen release and structural changes in TiO<sub>2</sub> films during photocatalytic oxidation have also been carried out using the same in situ setup [52].

L. Zhang et al. employed atomic resolution ETEM to study the structural evolution of anatase nanoparticles under 1 Torr of water vapor and broadband light illumination with a total intensity of 1430 mW/cm<sup>2</sup> [36]. An in situ heating holder was also used to provide a temperature of 150 °C to simulate the vapor-phase water splitting (Fig. 6.19a). During this in situ reaction procedure triggered by light illumination, an amorphous phase with a thickness of about one to two monolayers occurs in the initially crystalline surface (Fig. 6.19b). Further, EELS and X-ray photoelectron spectroscopy (XPS) characterization both reveal that the oxidation state of titanium in the surface amorphous layer is +3, while in the bulk is +4 (Fig. 6.19c, d). The amorphous layer remained stable with no thickness increase over time. This study is the first atomic resolution study on the surface evolution of anatase nanocrystals under photocatalytic splitting of water. This system was also utilized for in situ characterization of other photocatalysts under different environmental conditions [53, 54].

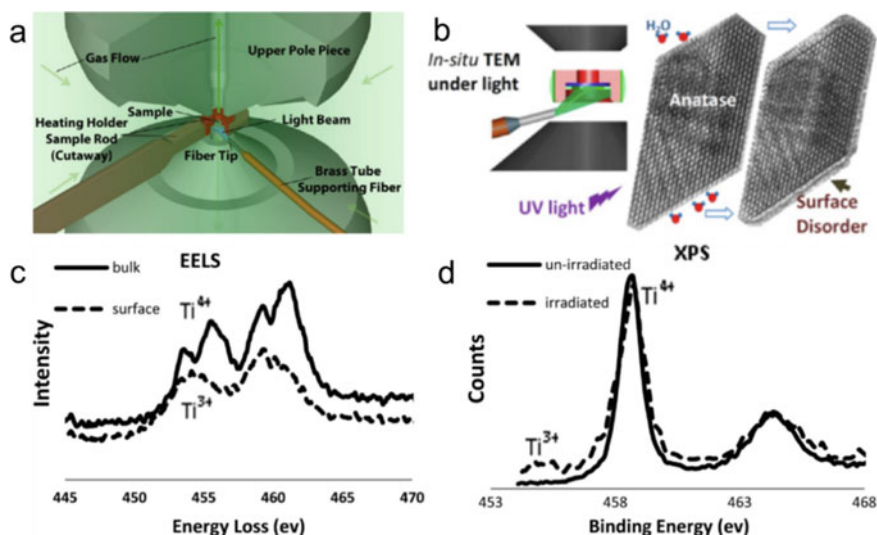


**Fig. 6.19** **a** Schematic diagram of an in situ TEM showing gases flowing into the sample chamber, an in situ heating holder for temperature control, and an optical fiber supported by a brass tube perpendicular to the sample rod for light illumination. **b** Surface disorder occurs in TiO<sub>2</sub> anatase nanocrystals under in situ UV light illumination and H<sub>2</sub>O gas environment when photocatalytic splitting of water occurs. **c** EELS spectra from the surface and bulk of the irradiated anatase samples. **d** XPS spectra of the irradiated and unirradiated anatase samples (reproduced with permission from Ref. [36], Copyright 2013, American Chemical Society)

F. Cavalca et al. developed two kinds of in situ TEM holders for realization of the photocatalytic reaction inside an ETEM [26]. One used a laser diode casing and a two-lens optical system that can guide light emitted from the laser diode onto the sample position. The other used fibers as light-paths to introduce light from external light sources. An in situ observation of photodeposition of Pt nanoparticles was carried out using this in situ TEM holder combined with ETEM (Fig. 6.20). The H<sub>2</sub>PtCl<sub>6</sub> vapor reacted on the surface of the GaN:ZnO particle, which is a highly active photocatalyst for water splitting under visible light exposure. After 4-h illumination with 405 nm wavelength and an intensity of 6 W cm<sup>-2</sup>, Pt nanoparticles appeared homogeneously on the surface of the GaN:ZnO with the disappearance of the amorphous layer. Similar work on photodeposition of Au nanoparticles on TiO<sub>2</sub> under UV light was also reported using a specimen chamber with an introduced optical fiber [55].

With the in situ TEM holder developed to contain fibers for light illumination, F. Cavalca et al. then carried out in situ observation of the photoreduction of Cu<sub>2</sub>O to metallic Cu under water vapor and illumination with 405 nm light at 6 W/cm<sup>2</sup> inside the ETEM [56]. The shape and morphology changes were obvious during the reaction, which was directly revealed by TEM-BF images (Fig. 6.21a–f). Selection area electron diffraction (SAED) was also used for structural analysis. As shown in Figs. 6.21g–l, a new (111) reflection of individual Cu grains gradually appeared with increased extent of reaction until exposed to UV light and water vapor for 75 min.

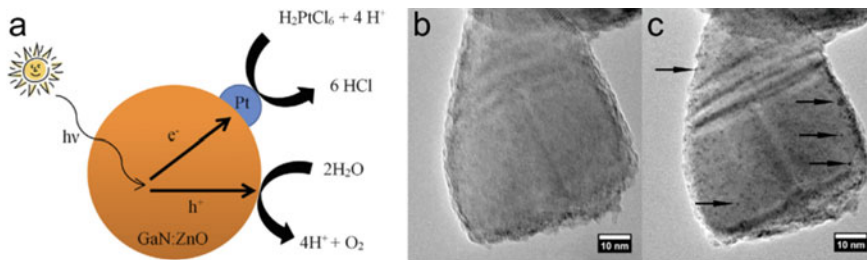


**Fig. 6.20** **a** Schematic sketch of the Pt photodeposition process. Light generates an electron–hole pair in the GaN:ZnO photocatalyst. Electrons and holes migrate to the surface and activate reactions with the surrounding chemical species. The electrons are responsible for the Pt precursor decomposition, while the holes drive the water oxidation reaction. **b**, **c** Bright-field TEM images of a GaN:ZnO particle **b** before and **c** after reaction in 5 mbar H<sub>2</sub>O and with 6 W cm<sup>-2</sup> light at a wavelength of 405 nm. The two images were acquired in vacuum, and the reaction was carried out in the absence of the electron beam. The arrows in **c** show some of the deposited Pt nanoparticles (reproduced with permission from Ref. [26], Copyright 2012, IOP Publishing)

This study provides a time-resolved systematic analysis of the light-activated reaction which demonstrates the reduction process of Cu<sub>2</sub>O into Cu, as well as giving further insight into the photoreduction reaction mechanisms.

### 6.3.2 PL and CL

Semiconducting materials, such as ZnO, AlN, and GaN, have been widely studied due to their unique optical and electronic properties for fabricating various optoelectronic devices including field effect transistors, LEDs, photodetectors, etc. [19, 57–59] TEM combined with in situ illumination/detection can provide us with immediate experimental evidence and profound understanding by correlating the microstructure (morphology, crystal orientation, atomic structure, etc.) with the optical and electronic properties of lattice defects in semiconducting materials by measuring the PL and CL [20, 60]. Besides, EELS, which is used to study optical properties such as light extinction and scattering, can be simultaneously available and thus provide complementary information with respect to CL during in situ studies [61–63]. Therefore, we could establish a direct correlation between structural properties and functional optical properties of semiconducting materials by means of in situ TEM optical analysis.

The selective photo-excitation of a single dislocation can be demonstrated by the use of the near-field light probe [20, 21]. For a diamond film (Fig. 6.22a), the PL, CL, and Raman spectra can be acquired from the same specific region as shown in Fig. 6.22. From Fig. 6.22c, d, the observed Raman spectrum with a peak at 1332 cm<sup>-1</sup> and a zero-phonon PL spectrum with a peak at 2.156 eV, as well as its phonon replicas, are correlated with nitrogen impurities and vacancies because of the variation of

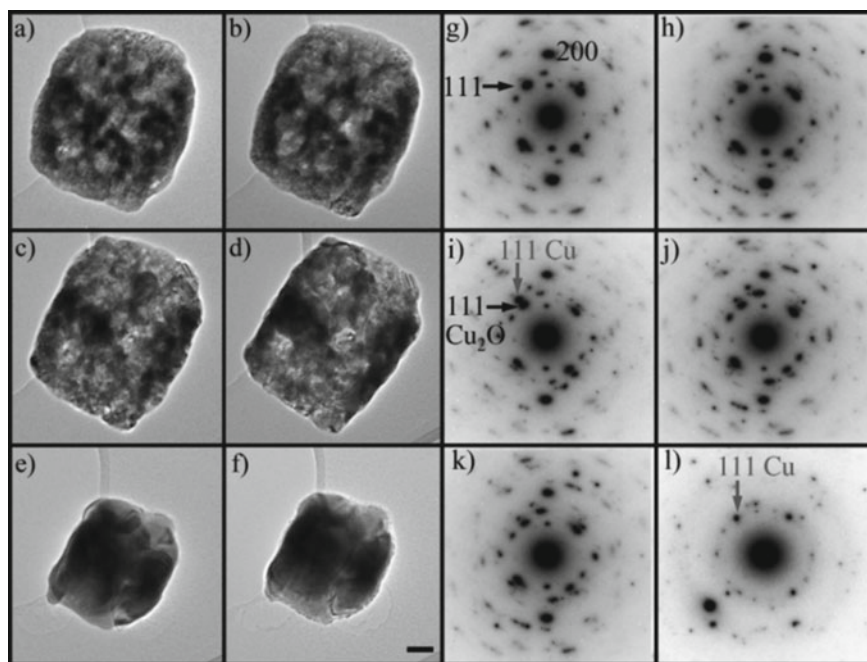


**Fig. 6.21** a–f TEM-BF images and g–l corresponding SAED patterns of  $\text{Cu}_2\text{O}$  particles inside in situ ETEM before and during the photocatalytic reaction (every 15 min from 0 to 75 min). Obvious changes can be found on the shape and morphology of particles. New reflections for metallic Cu also appeared in SAED patterns. Scale bar is 50 nm (reproduced with permission from Ref. [56], Copyright 2013, John Wiley and Sons)

the zero-phonon lines obtained at different strains and the absence of local mode structures. The CL spectrum acquired from the same region (Fig. 6.22e) shows similar features to the PL, which should also be associated to the nitrogen impurities and vacancies. However, the signal-to-noise ratio of the CL spectrum is better than that of the PL spectrum.

The newly developed parallel-detection-mode CL-STEM by S. Lim et al. (Fig. 6.23a), which can minimize the impact of electron beam irradiation damage, can also correlate optical properties with the microstructures of GaN/AlGaN nanowires [60]. Figure 6.23b shows the observed CL spectrum with a peak at 365 nm corresponding to the near-band-edge (NBE) emission of GaN at room temperature. Its intensity gradually diminished as the specimen was cooled. The new peak at 378 nm (110 K) could be considered as donor–acceptor pair (DAP) emission as well as LO-phonon replicas, which is related to the acceptor impurities or defects like the SiN or  $\text{V}_{\text{Ga}}\text{-O}$  complexes. Figure 6.23d, e indicates that two kinds of emissions were generated from the core, suggesting the uniform distribution of dopants with small variations. From Fig. 6.23f, the DAP emission was quenched at the corners of the

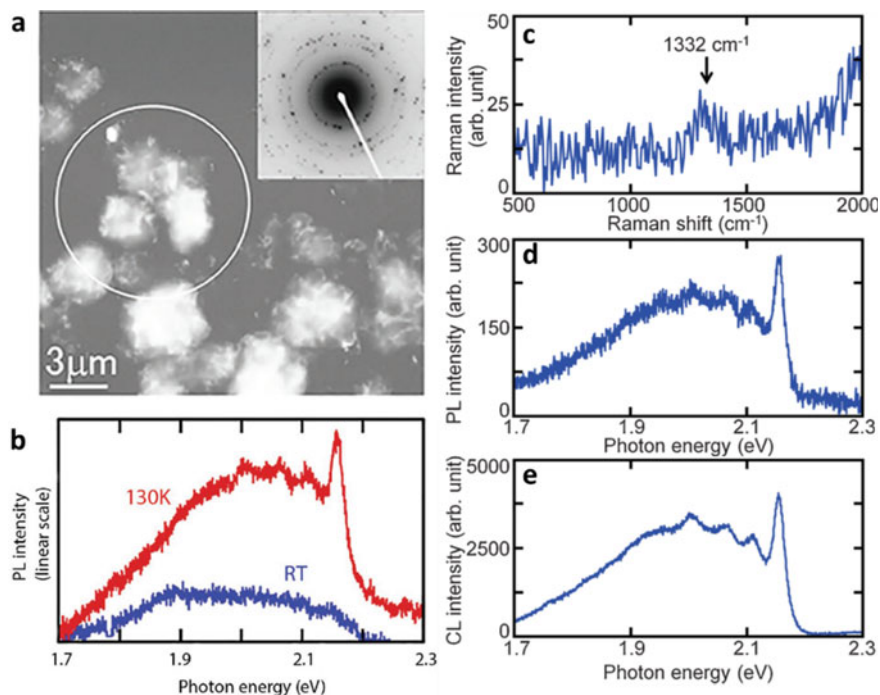


**Fig. 6.22** **a** A TEM image and **b** the corresponding PL spectrum taken from the area of a diamond film in **a** (reproduced with permission from Ref. [21], Copyright 2014, Elsevier) **c** Raman, **d** PL, and **e** CL spectra taken from the same area of a CVD-grown diamond film (about 500 nm thick) (reproduced with permission from Ref. [20], Copyright 2012, The Japan Society of Applied Physics)

nanowire, which may result from piezoelectric and spontaneous polarization in the shell.

Besides nanowires, the high spatial resolution of STEM-CL also enables the ability to observe InGaN/GaN quantum wells (QWs) in LED devices. The reduced quantum confined Stark effect in InGaN/GaN QWs LEDs was reported using such a technique. Figure 6.24 shows six spectral features related to QWs1-6. The CL spatial resolution is much smaller than the diffusion length of the carriers ( $\sim 100$  nm for GaN, InGaN) that limits the overall resolution, and the improved CL spatial resolution can be attributed to the carrier's quantum confinement. Similar work on GaN quantum disks and red quantum dots have also been studied [64, 65].

Through the combination of EELS and CL measurements by A. Losquin et al. (Fig. 6.25a), nanometric-scale extinction and scattering phenomena were unveiled [61]. From Fig. 6.25 b, the EELS spectrum has a significant blue shift with respect to the CL spectrum. Analogous shifts and broadening have been recorded on different specimens, which lead to the association of the phenomena of extinction and scattering. The calculations of EELS and CL spectra in Fig. 6.25c show that EELS signal corresponds to extinction, while CL signal corresponds to scattering, between which

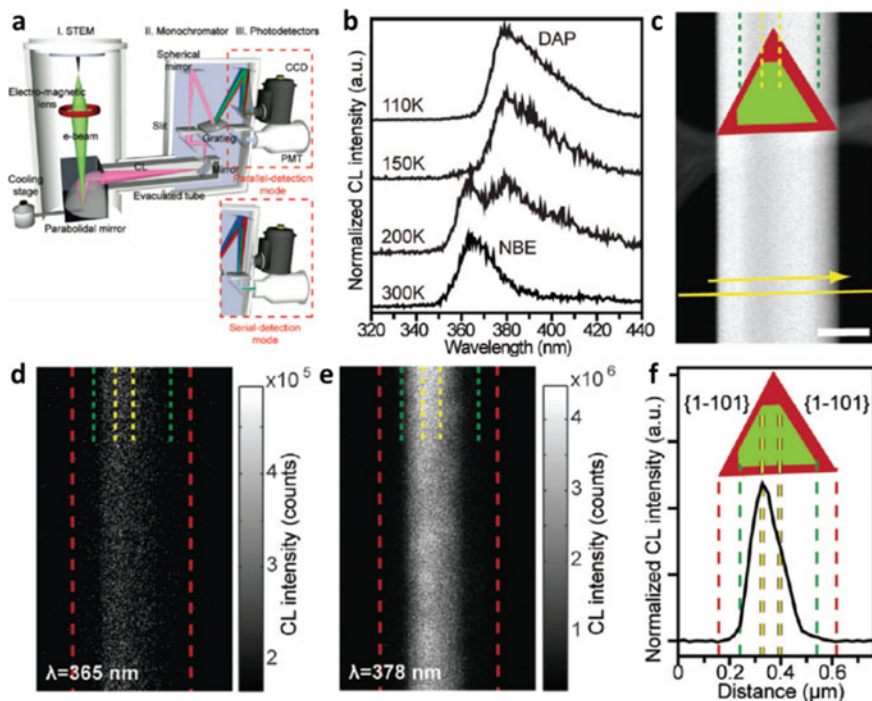


**Fig. 6.23** **a** A schematic diagram of a type of CL-STEM apparatus. **b–f** Structural and optical properties of an individual GaN/AlGaN core-shell (CS) nanowire. **b** Normalized CL spectra obtained at different temperatures. **c** Dark-field STEM image of a CS nanowire structure. **d, e** Monochromatic CL images taken at 365 nm (300 K) and 378 nm (110 K). **f** Normalized CL intensity profile obtained along the yellow line in **c** of the emission at 378 nm (reproduced with permission from Ref. [60], Copyright 2009, American Chemical Society)

there is a blue shift. Similar work on surface plasmon modes of  $\text{Bi}_2\text{Te}_3$  nanoplates and light-matter interactions of nanoparticles have also been studied by EELS and CL [62, 63].

By using a Gatan Vulcan CL holder, the relationship between the interlayer twist and local light excitation of chiral van der Waals (vdW) nanowires was determined (Fig. 6.26a) [66]. Figure 6.26b, c shows synchronous changes of parameters including FWHM, wavelength, and intensity as a result of the accumulated twist. The changes in the above CL spectra originate from the rotation of the chiral vdW layers or changes in electronic structure of the nanowire. Similar work on luminescence in ZnO nanostructures and nanosized cubic  $\text{Y}_2\text{O}_3:\text{Tb}^{3+}$  have also been studied using Gatan Vulcan CL holders [58, 67].

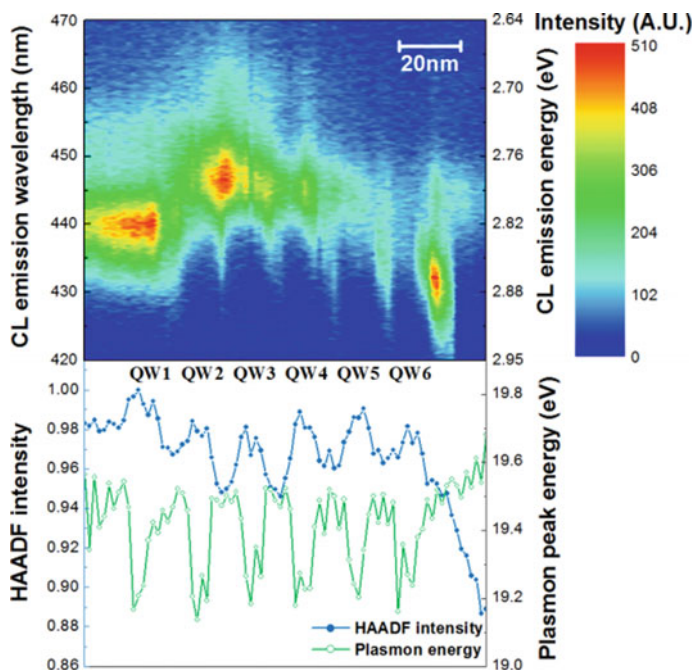


**Fig. 6.24** The CL spectral profile, HAADF intensity profile, and plasmon peak energy profile across the InGaN/GaN QWs (reproduced with permission from Ref. [57], Copyright 2015, American Chemical Society)

### 6.3.3 Photocurrent

Photoelectric conversion is the process of directly converting luminous energy into electric energy through a photovoltaic process. Normal methods to achieve photoelectric conversion include photoelectric devices such as solar cells [68, 69], photodetectors [70, 71], and photodiodes [72]. Semiconductive materials, such as  $\text{TiO}_2$  [73], CdS [37, 74], ZnO [27, 28], Si [75], and perovskite [76], are used in diverse photoelectric devices because of their suitable bandgaps and unique electronic, optical, and piezoelectric properties. Measuring the photocurrents of these materials is of great help in studying the factors that affect the photoelectric performance. Based on this, researchers have developed a variety of methods for achieving the measurement of photocurrents inside the TEM, such as introducing optical fibers into the holder, designing MEMS systems, and affixing LEDs on the holder. Some effective work has been carried out through these methods and important results have been gained.

C. Zhang et al. upgraded an optical fiber-compatible TEM holder and carried out a series of work on CdS nanowires [77], CdS/ZnO heterostructures [78], and CdS/p-Si nanowire heterojunctions [37]. A comparative experiment between a CdS nanowire and CdS/ZnO heterostructure on their photoelectric response shows in  $I$ - $V$  characteristics measured by sweeping the voltage from  $-5$  to  $5$  V with a 405 nm

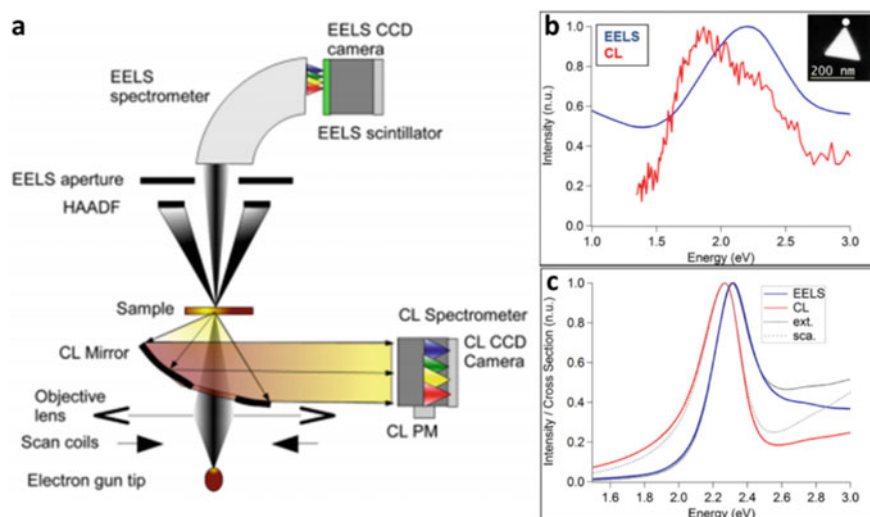


**Fig. 6.25** **a** A schematic diagram of a scanning transmission electron microscope (STEM) fitted with homemade EELS and CL systems. **b** EELS and CL spectra obtained at the tip of a gold prism (edge length: 140 nm). **c** Calculated extinction, scattering, EELS, and CL spectra of a small nanoprism (length: 50 nm; thickness: 50 nm) (reproduced with permission from Ref. [61], Copyright 2015, American Chemical Society)

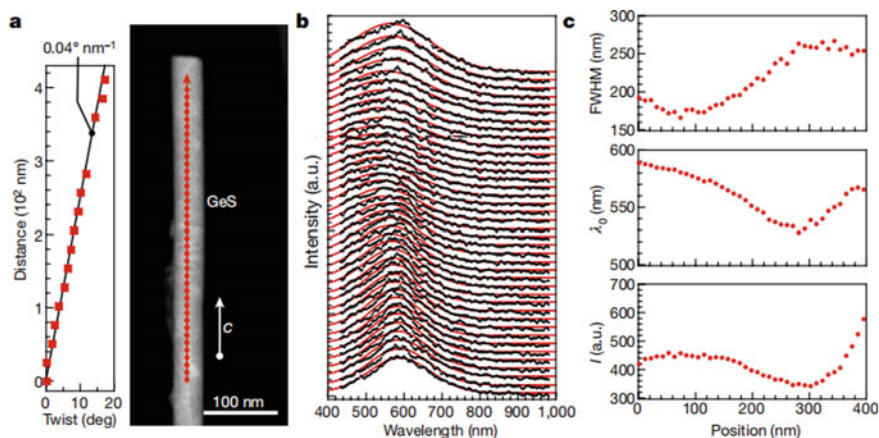


**Fig. 6.26** **a** A STEM-HAADF image and a plot of cumulative twist of a GeS nanowire. **b** The CL spectra taken at marked points **a** at room temperature. **c** The FWHM, center wavelength ( $\lambda_0$ ), and intensity ( $I$ ) of the Gaussian fits in **b** (reproduced with permission from Ref. [66], Copyright 2019, Springer Nature)

light on and off, respectively (Fig. 6.27). These indicate the heterostructures show a dramatic photocurrent to dark current ratio and responsivity compared to CdS nanowires. The study on CdS/p-Si nanowire heterojunctions shows a photocurrent saturation effect as well as a good selectivity of light frequencies. Similar work on bending ZnO nanowires have also been studied revealing photocurrent spectra splitting [79], photoconduction, and photoresponse behavior [27, 28] by using an opto-TEM-STM holder with an optical fiber or LED.

Y. Zhu et al. developed a multimodal optical nanoprobe (MON) in cooperation with Nanofactory Instruments AB [80]. The nanoprobe has two channels that pass external light sources (typically 370 nm–2400 nm) to the sample (Fig. 6.28a). These two channels distribute on each side of the sample. In addition to this, two adjustable mirrors help focus input light onto the sample or collect and reflect scattered light from sample to channel for analysis. The MON system also contains a nanomanipulator which can provide fine and coarse motion in three dimensional. Figure 6.28b shows

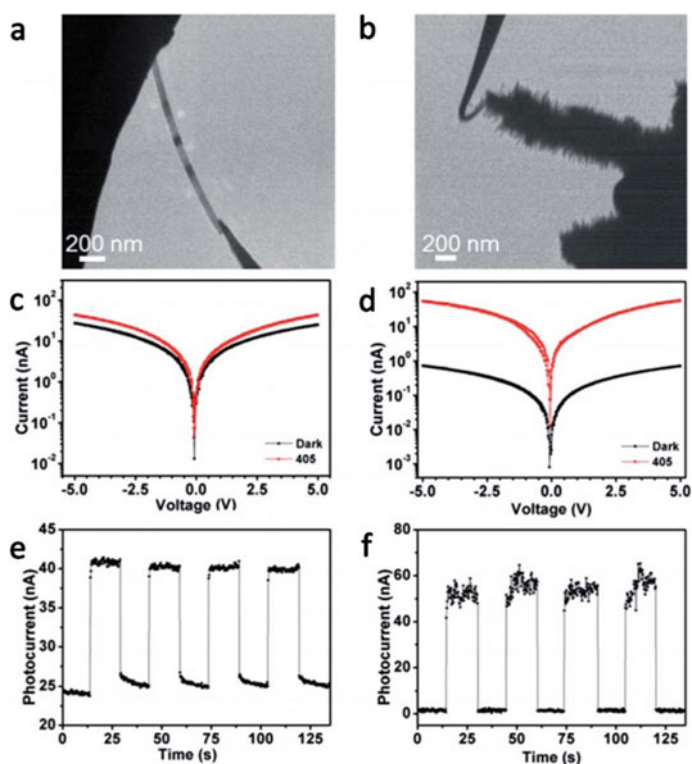


**Fig. 6.27** a, b TEM images of an individual CdS nanobelt (a) and an individual CdS/ZnO heterostructure (b). c, d Corresponding photocurrent and dark current of the individual CdS nanobelt and the individual CdS/ZnO heterostructure. e, f Corresponding photocurrent responses of the individual CdS nanobelt photodetector and individual CdS/ZnO heterostructure photodetector (reproduced with permission from Ref. [78], Copyright 2015, IOP Publishing)

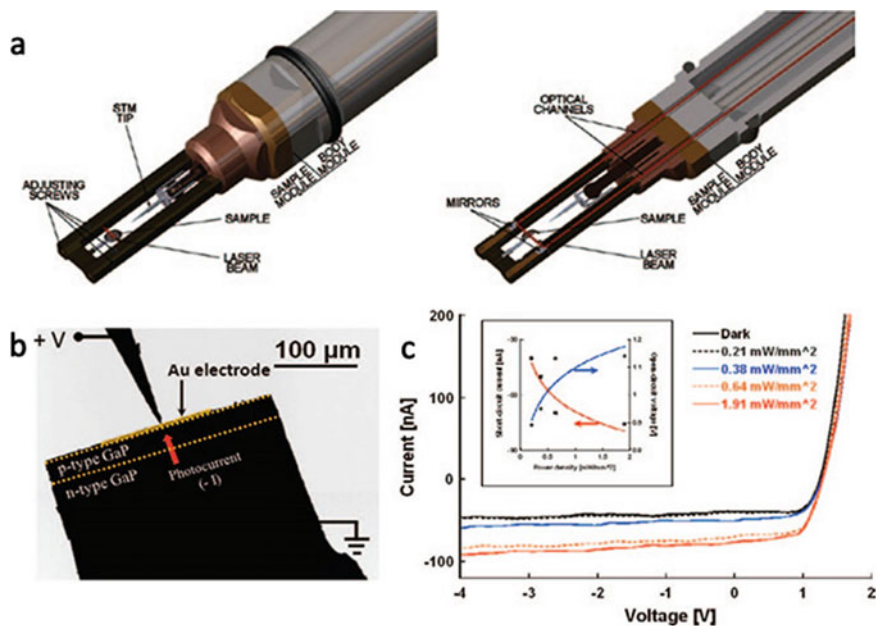


**Fig. 6.28** **a** A view of the nanoprobe. **b** TEM image of a commercial LED. **c** Current–voltage ( $I$ – $V$ ) curve with a 454 nm laser. The inset shows a decrease of  $I_{sc}$  and increase of  $V_{oc}$  with the power density of the laser (reproduced with permission from Ref. [80], Copyright 2012, Cambridge University Press)

the TEM images of a commercial LED contacted by a movable tungsten probe. Dark current and photocurrent (Fig. 6.28c) were measured with a 454 nm laser. The short-circuit current ( $I_{sc}$ ) decreases and open-circuit voltage ( $V_{oc}$ ) increases with the power density of the laser. This MON system can achieve more reliable and accurate photovoltaic measurements.

S. Cai et al. adapted an in situ optoelectrical MEMS system for photoelectrical measurement of a wide range of samples such as one-dimensional (1D) nanowires and FIB-prepared cross-sectional samples (Fig. 6.29) [34]. Figure 6.29c, d shows TEM images of a single 3C-SiC nanowire in Fig. 6.29a and the corresponding selected area electron diffraction (SAED) pattern confirms the crystalline-zinc-blended crystal structure along the  $[-110]$  zone axis. Photoconductivity was performed with an external bias ranging from  $-20$  to  $20$  V where the current increased when the LED switched on. The photocurrent at  $\pm 20$  V external bias approximately doubled compared with that in the dark (Fig. 6.29e). The nanowire exhibited simultaneous light-sensing capability where the forward current and photoconductivity increased. By applying a 10-mA forward current square wave, the SiC nanowire at 20-V bias exhibited a fast-current response to the light intensity change (Fig. 6.29f).

Work by H. Dong et al. constructed a single  $\text{TiO}_2$ -nanowire/CdSe-QD heterojunction solar cell (QDHSC) within a custom-designed TEM-STM holder to understand

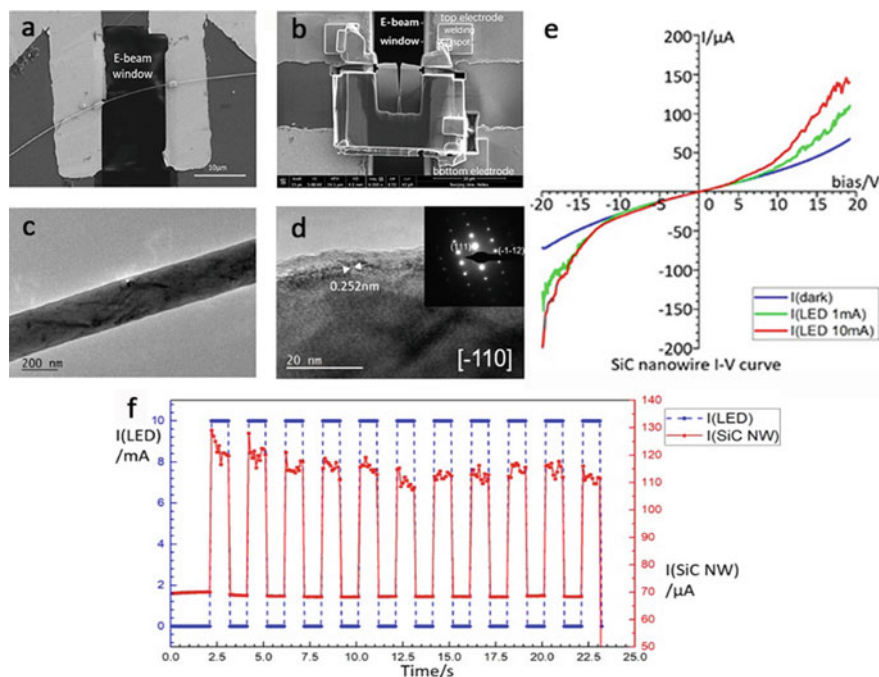


**Fig. 6.29** **a** A SiC nanowire welded to both micro-electrodes with Pt deposition and bridging over the viewing window in the middle. **b** A cross-sectional TEM sample was fabricated by FIB system and connected to the MEMS chip. **c** Low-magnification TEM and **d** HRTEM images of SiC nanowires welded on the chip. The corresponding SAED pattern (inset) shows the  $[-110]$  zone axis. **e** In situ I-V curve of SiC nanowire with LED ON/OFF measured with electron beam blanked. **f** Photoconductivity measurements of SiC nanowire with 20-V bias voltage using a series of square waves from 1 to 10 mA: forward current to the LED (blue) and photocurrent generated in the nanowire (red) (reproduced with permission from Ref. [34], Copyright 2018, Elsevier)

the effect of interfaces and defects on the photovoltaic performance of QDHSC [30]. This QDHSC consists of an individual  $\text{TiO}_2$  nanowire with uniformly coated CdSe QDs and contact electrodes Pt and Cu (Fig. 6.30a, b). The QDHSC is exposed by an LED whose power intensity is  $3 \text{ mW/cm}^2$ . The TEM images and fast Fourier transformation pattern reveal the crystal information of the  $\text{TiO}_2$  nanowire and CdSe-QD. Then the photocurrent and dark current were measured, and the power conversion efficiency (PCE) of the solar cell was 27.7% with a white light. As shown in Fig. 6.30c–e, direct in situ control over different interface areas ( $S$ ) was achieved by selecting different nanowire lengths ( $L$ ) through the movement of the Pt electrode. Simultaneously, a change of photocurrent density occurs with different interfacial areas (Fig. 6.30f). More data were fitted by a modified Shockley–Read–Hall recombination model (Fig. 6.30g). It is noteworthy that photocurrent densities with larger interfacial areas show an inverse trend. In general, a larger interfacial area provides

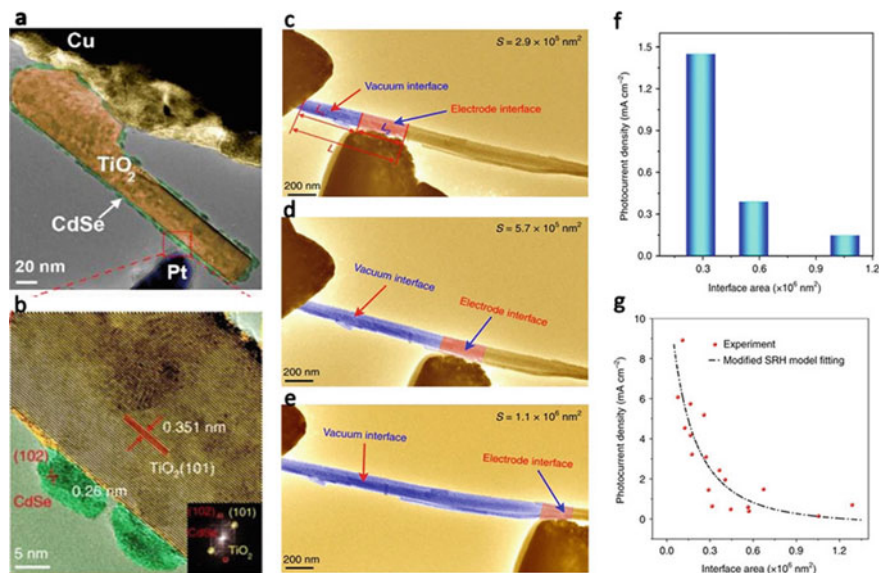


**Fig. 6.30** TEM image **a** and HRTEM image **b** of an individual TiO<sub>2</sub> nanowire with CdSe QDs. The inset of **b** is a corresponding FFT pattern. **c–e** TEM images of QDHSC with different interfacial areas (blue and red areas). **f** Histogram of the photocurrent density from the different interface areas in **c–e**. **g** Statistical distribution of the photocurrent density. Fitted data to the modified Shockley–Read–Hall (SRH) model as a function of the interface area (reproduced with permission from Ref. [30], Copyright 2019, Springer Nature)

a larger number of defects, which trap more photoelectrons. Thus, photogenerated carriers suffer a great possibility of being lost during the transport process.

The open-voltage data were fitted as a function of interfacial area using a modified Shockley–Read–Hall model, which indicates the  $V_{oc}$  first experiences a sharp increase with  $S$  below a value of  $3 \times 10^5 \text{ nm}^2$  and levels off with further increase in  $S$  (Fig. 6.31a). The increase in  $V_{oc}$  is mainly attributed to the decreased current density with increasing interface area. Figure 6.31b shows the statistical distribution of the PCE as a function of the interface area. This provides evidence to elucidate the relationship between the interfaces and the photovoltaic performance and acts as a guideline to optimize the parameters and maximize the efficiency of the corresponding solar cells.

## 6.4 Future and Opportunities

The fast development of detector and imaging techniques of TEMs has brought more opportunities for material researchers. For example, ultrafast and direct electron cameras greatly improve the efficiency and time resolution of conventional TEMs.

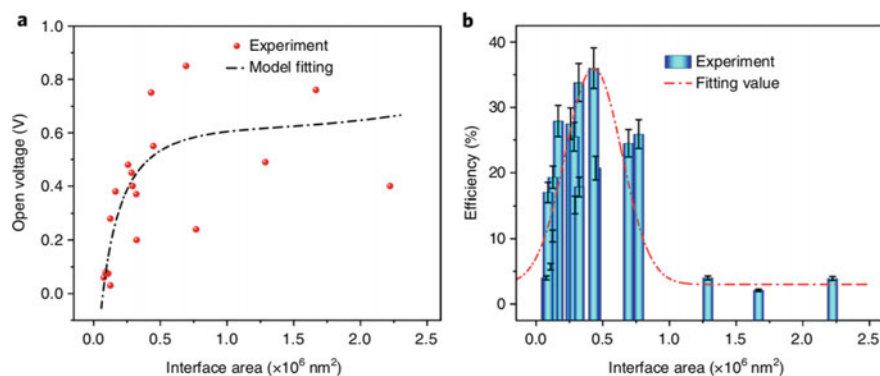


**Fig. 6.31** **a** Statistical distribution of the  $V_{oc}$ . The fit of the data to the modified Shockley–Read–Hall (SRH) model as a function of interfacial area. **b** Statistical distribution of the PCE as a function of the interfacial area of the QDHSC (reproduced with permission from Ref. [30], Copyright 2019, Springer Nature)

Differential phase contrast (DPC) and four-dimensional STEM (4D-STEM) not only realize functions of traditional STEM, but also provide information like electric field, potential, charge density, and magnetic field [81]. Electron tomography and ptychography have become promising solutions for three-dimensional (3D) structures and light atom characterization with high spatial resolution, respectively. These significant technical improvements will further benefit future applications of in situ optical TEM.

Advanced detectors will stimulate the improvement of both in situ TEM characterizations and in situ facilities. The raising application of ultrafast detectors with time resolution up to  $\sim 1 \mu\text{s}$  enables a much more accurate in situ record of structure evolution during reaction processes, which is important for detailed characterization of the photoresponse of photocatalysts and semiconductors. Combined with DPC and 4D-STEM techniques based on ultrafast camera, in situ characterization of light-induced electric field, potential, and charge density evolution is expected to be realized. Direct electron cameras have much better quantum efficiency than traditional cameras, which allows high-quality imaging with extremely low electron dose rates. This can extend the sample adaptability for in situ optical TEM observation such as electron-sensitive metal–organic frameworks (MOF) and covalent organic framework (COF), which have attracted expansive attention as novel catalyst supports and have been utilized for photocatalyst development [82, 83], and may also provide possible solutions for in situ photocurrent measurements of electron-sensitive organic–inorganic hybrid perovskites [84].

Based on the growing quantum efficiency of light detectors, the improvement of in situ PL and CL detection systems will provide better data quality, especially for nanoscale samples, where single-photon detection can be realized one day. High efficiency detection can also help reduce dose rates to avoid electron beam radiation damage and improve acquisition speed for atomically resolved spectroscopy images.

Nevertheless, in situ PL and CL detection in TEM is expected to play more important roles in the development of novel semiconducting materials and devices. In addition, the small-sized, high accuracy light detector will also help the calibration of in situ illumination systems, which is essential for quantitative analysis of sample properties.

The combination of in situ optical measurement and computational reconstruction techniques will bring more details about sample structures and chemical states. Electron tomography can acquire 3D structural information of nanomaterials, and the newly developed 4D electron tomography technique has successfully realized time-resolved 3D spatial resolution [85]. This may realize in situ optical measurements as promising solutions for in situ analysis of active sites and fine 3D structure evolution during photocatalytic reactions. Electron ptychography can achieve better contrast on light atoms [86] and provide more flexibility for the usage of electron signals for image reconstruction simultaneously with EELS acquisition [87]. An unprecedented complete understanding of in situ behaviors can be expected with the continued improvement of both the hardware and software of electron microscopy.

## References

1. Zhai T, Li L, Wang X, Fang X, Bando Y, Golberg D (2010) Recent developments in one-dimensional inorganic nanostructures for photodetectors. *Adv Func Mater* 20(24):4233–4248. <https://doi.org/10.1002/adfm.201001259>
2. Jariwala D, Sangwan VK, Lauhon LJ, Marks TJ, Hersam MC (2013) Carbon nanomaterials for electronics, optoelectronics, photovoltaics, and sensing. *Chem Soc Rev* 42(7):2824–2860. <https://doi.org/10.1039/c2cs35335k>
3. Khalid NR, Majid A, Tahir MB, Niaz NA, Khalid S (2017) Carbonaceous-TiO<sub>2</sub> nanomaterials for photocatalytic degradation of pollutants: a review. *Ceram Int* 43(17):14552–14571. <https://doi.org/10.1016/j.ceramint.2017.08.143>
4. Dincer I, Acar C (2015) A review on clean energy solutions for better sustainability. *Int J Energy Res* 39(5):585–606. <https://doi.org/10.1002/er.3329>
5. Li Y, Qian F, Xiang J, Lieber CM (2006) Nanowire electronic and optoelectronic devices. *Mater Today* 9(10):18–27. [https://doi.org/10.1016/S1369-7021\(06\)71650-9](https://doi.org/10.1016/S1369-7021(06)71650-9)
6. Kim Judy S, LaGrange T, Reed Bryan W, Taheri Mitra L, Armstrong Michael R, King Wayne E, Browning Nigel D, Campbell Geoffrey H (2008) Imaging of transient structures using nanosecond in situ TEM. *Science* 321(5895):1472–1475. <https://doi.org/10.1126/science.1161517>
7. Golberg D, Costa PMFJ, Wang M-S, Wei X, Tang D-M, Xu Z, Huang Y, Gautam UK, Liu B, Zeng H, Kawamoto N, Zhi C, Mitome M, Bando Y (2012) Nanomaterial engineering and property studies in a transmission electron microscope. *Adv Mater* 24(2):177–194. <https://doi.org/10.1002/adma.201102579>
8. Ji D, Cai S, Paudel TR, Sun H, Zhang C, Han L, Wei Y, Zang Y, Gu M, Zhang Y, Gao W, Huyan H, Guo W, Wu D, Gu Z, Tsymbal EY, Wang P, Nie Y, Pan X (2019) Freestanding crystalline oxide perovskites down to the monolayer limit. *Nature* 570(7759):87–90. <https://doi.org/10.1038/s41586-019-1255-7>
9. Dou Z, Chen Z, Li N, Yang S, Yu Z, Sun Y, Li Y, Liu B, Luo Q, Ma T, Liao L, Liu Z, Gao P (2019) Atomic mechanism of strong interactions at the graphene/sapphire interface. *Nat Commun* 10(1):5013. <https://doi.org/10.1038/s41467-019-13023-6>

10. Sun Y, Abid AY, Tan C, Ren C, Li M, Li N, Chen P, Li Y, Zhang J, Zhong X, Wang J, Liao M, Liu K, Bai X, Zhou Y, Yu D, Gao P (2019) Subunit cell-level measurement of polarization in an individual polar vortex. *Sci Adv* 5(11):eaav4355. <https://doi.org/10.1126/sciadv.aav4355>
11. Zhu C, Yu M, Zhou J, He Y, Zeng Q, Deng Y, Guo S, Xu M, Shi J, Zhou W, Sun L, Wang L, Hu Z, Zhang Z, Guo W, Liu Z (2020) Strain-driven growth of ultra-long two-dimensional nano-channels. *Nat Commun* 11(1):772. <https://doi.org/10.1038/s41467-020-14521-8>
12. Li W, Zhou J, Cai S, Yu Z, Zhang J, Fang N, Li T, Wu Y, Chen T, Xie X, Ma H, Yan K, Dai N, Wu X, Zhao H, Wang Z, He D, Pan L, Shi Y, Wang P, Chen W, Nagashio K, Duan X, Wang X (2019) Uniform and ultrathin high- $\kappa$  gate dielectrics for two-dimensional electronic devices. *Nat Electron* 2(12):563–571. <https://doi.org/10.1038/s41928-019-0334-y>
13. Chen Z, Zhang X, Dou Z, Wei T, Liu Z, Qi Y, Ci H, Wang Y, Li Y, Chang H, Yan J, Yang S, Zhang Y, Wang J, Gao P, Li J, Liu Z (2018) High-brightness blue light-emitting diodes enabled by a directly grown graphene buffer layer. *Adv Mater* 30(30):1801608. <https://doi.org/10.1002/adma.201801608>
14. Chen Z, Liu Z, Wei T, Yang S, Dou Z, Wang Y, Ci H, Chang H, Qi Y, Yan J, Wang J, Zhang Y, Gao P, Li J, Liu Z (2019) Improved epitaxy of AlN film for deep-ultraviolet light-emitting diodes enabled by graphene. *Adv Mater* 31(23):1807345. <https://doi.org/10.1002/adma.201807345>
15. Wan S, Zhu Z, Yin K, Su S, Bi H, Xu T, Zhang H, Shi Z, He L, Sun L (2018) A highly skin-conformal and biodegradable graphene-based strain sensor. *Small Methods* 2(10):1700374. <https://doi.org/10.1002/smt.201700374>
16. Golberg D, Zhang C, Xu Z (2014) Cubic lattice nanosheets: thickness-driven light emission. *ACS Nano* 8(7):6516–6519. <https://doi.org/10.1021/nn502999g>
17. Suzuki K, Ichihara M, Takeuchi S, Nakagawa K, Maeda K, Iwanaga H (1984) In situ TEM observation of dislocation motion in II–VI compounds. *Philos Mag A* 49(3):451–461. <https://doi.org/10.1080/01418618408233287>
18. Ohno Y, Takeda S (1995) A new apparatus for in situ photoluminescence spectroscopy in a transmission electron microscope. *Rev Sci Instrum* 66(10):4866–4869. <https://doi.org/10.1063/1.1146166>
19. Ohno Y, Taishi T, Yonenaga I (2009) In situ analysis of optoelectronic properties of dislocations in ZnO in TEM observations. *Phys Status Solidi (a)* 206(8):1904–1911. <https://doi.org/10.1002/pspa.200881466>
20. Ohno Y (2012) Development of an apparatus for in-situ near-field photoexcitation in a transmission electron microscope. *Appl Phys Express* 5(12):125204. <https://doi.org/10.1143/apex.5.125204>
21. Ohno Y, Yonenaga I (2014) In-situ micro and near-field photo-excitation under transmission electron microscopy. *Appl Surf Sci* 302:29–31. <https://doi.org/10.1016/j.apsusc.2013.11.061>
22. Picher M, Mazzucco S, Blankenship S, Sharma R (2015) Vibrational and optical spectroscopies integrated with environmental transmission electron microscopy. *Ultramicroscopy* 150:10–15. <https://doi.org/10.1016/j.ultramic.2014.11.023>
23. Miller BK, Crozier PA (2013) System for in situ UV-visible illumination of environmental transmission electron microscopy samples. *Microsc Microanal* 19(2):461–469. <https://doi.org/10.1017/S1431927612014122>
24. Tanabe T, Muto S, Tohtake S (2002) Development of new TEM specimen holder for cathodoluminescence detection. *J Electron Microsc* 51(5):311–313. <https://doi.org/10.1093/jmicro/51.5.311>
25. Shindo D, Takahashi K, Murakami Y, Yamazaki K, Deguchi S, Suga H, Kondo Y (2009) Development of a multifunctional TEM specimen holder equipped with a piezodriving probe and a laser irradiation port. *J Electron Microsc* 58(4):245–249. <https://doi.org/10.1093/jmicro/dfp018>
26. Cavalca F, Laursen AB, Kardynal BE, Dunin-Borkowski RE, Dahl S, Wagner JB, Hansen TW (2012) In situ transmission electron microscopy of light-induced photocatalytic reactions. *Nanotechnology* 23(7):075705. <https://doi.org/10.1088/0957-4484/23/7/075705>

27. Gao P, Wang ZZ, Liu KH, Xu Z, Wang WL, Bai XD, Wang EG (2009) Photoconducting response on bending of individual ZnO nanowires. *J Mater Chem* 19(7):1002–1005. <https://doi.org/10.1039/b816791e>
28. Yang S, Wang L, Tian X, Xu Z, Wang W, Bai X, Wang E (2012) The piezotronic effect of zinc oxide nanowires studied by in situ TEM. *Adv Mater* 24(34):4676–4682. <https://doi.org/10.1002/adma.201104420>
29. Dong H, Xu T, Sun Z, Zhang Q, Wu X, He L, Xu F, Sun L (2018) Simultaneous atomic-level visualization and high precision photocurrent measurements on photoelectric devices by in situ TEM. *RSC Adv* 8(2):948–953. <https://doi.org/10.1039/c7ra10696c>
30. Dong H, Xu F, Sun Z, Wu X, Zhang Q, Zhai Y, Tan XD, He L, Xu T, Zhang Z, Duan X, Sun L (2019) In situ interface engineering for probing the limit of quantum dot photovoltaic devices. *Nat Nanotechnol* 14(10):950–956. <https://doi.org/10.1038/s41565-019-0526-7>
31. Zhang M, Olson E, Twesten R, Wen J, Allen L, Robertson I, Petrov I (2005) In situ transmission electron microscopy studies enabled by microelectromechanical system technology. *J Mater Res* 20(7):1802–1807. <https://doi.org/10.1557/JMR.2005.0225>
32. Zhu Y, Espinosa HD (2005) An electromechanical material testing system for in situ electron microscopy and applications. *Proc Natl Acad Sci* 102(41):14503–14508. <https://doi.org/10.1073/pnas.0506544102>
33. Haque M, Espinosa H, Lee H (2010) MEMS for in situ testing—handling, actuation, loading, and displacement measurements. *MRS Bull* 35(5):375–381. <https://doi.org/10.1557/mrs2010.570>
34. Cai S, Gu C, Wei Y, Gu M, Pan X, Wang P (2018) Development of in situ optical–electrical MEMS platform for semiconductor characterization. *Ultramicroscopy* 194:57–63. <https://doi.org/10.1016/j.ultramic.2018.07.007>
35. Fernando JFS, Zhang C, Firestein KL, Golberg D (2017) Optical and optoelectronic property analysis of nanomaterials inside transmission electron microscope. *Small* 13(45):1701564. <https://doi.org/10.1002/smll.201701564>
36. Zhang L, Miller BK, Crozier PA (2013) Atomic level in situ observation of surface amorphization in anatase nanocrystals during light irradiation in water vapor. *Nano Lett* 13(2):679–684. <https://doi.org/10.1021/nl304333h>
37. Zhang C, Xu Z, Tian W, Tang D-M, Wang X, Bando Y, Fukata N, Golberg D (2015) In situ fabrication and optoelectronic analysis of axial CdS/p-Si nanowire heterojunctions in a high-resolution transmission electron microscope. *Nanotechnology* 26(15):154001. <https://doi.org/10.1088/0957-4484/26/15/154001>
38. Miller DR, Williams RE, Akbar SA, Morris PA, McComb DW (2017) STEM-cathodoluminescence of SnO<sub>2</sub> nanowires and powders. *Sens Actuators B Chem* 240:193–203. <https://doi.org/10.1016/j.snb.2016.08.145>
39. Vadai M, Angell DK, Hayee F, Sytwu K, Dionne JA (2018) In-situ observation of plasmon-controlled photocatalytic dehydrogenation of individual palladium nanoparticles. *Nat Commun* 9(1):4658. <https://doi.org/10.1038/s41467-018-07108-x>
40. Huang JY, Zhong L, Wang CM, Sullivan JP, Xu W, Zhang LQ, Mao SX, Hudak NS, Liu XH, Subramanian A, Fan H, Qi L, Kushima A, Li J (2010) In situ observation of the electrochemical lithiation of a single SnO<sub>2</sub> nanowire electrode. *Science* 330(6010):1515–1520. <https://doi.org/10.1126/science.1195628>
41. Yang Y, Gao P, Gaba S, Chang T, Pan X, Lu W (2012) Observation of conducting filament growth in nanoscale resistive memories. *Nat Commun* 3(1):732. <https://doi.org/10.1038/ncomms1737>
42. Liu Q, Sun J, Lv H, Long S, Yin K, Wan N, Li Y, Sun L, Liu M (2012) Real-time observation on dynamic growth/dissolution of conductive filaments in oxide-electrolyte-based ReRAM. *Adv Mater* 24(14):1844–1849. <https://doi.org/10.1002/adma.201104104>
43. Sun J, He L, Lo Y-C, Xu T, Bi H, Sun L, Zhang Z, Mao SX, Li J (2014) Liquid-like pseudoelasticity of sub-10-nm crystalline silver particles. *Nat Mater* 13(11):1007–1012. <https://doi.org/10.1038/nmat4105>

44. Costa PMFJ, Golberg D, Shen G, Mitome M, Bando Y (2008) ZnO low-dimensional structures: electrical properties measured inside a transmission electron microscope. *J Mater Sci* 43(4):1460–1470. <https://doi.org/10.1007/s10853-007-2307-1>
45. Grapes MD, LaGrange T, Friedman LH, Reed BW, Campbell GH, Weihs TP, LaVan DA (2014) Combining nanocalorimetry and dynamic transmission electron microscopy for in situ characterization of materials processes under rapid heating and cooling. *Rev Sci Instrum* 85(8):084902. <https://doi.org/10.1063/1.4892537>
46. Westenfelder B, Meyer JC, Biskupek J, Algara-Siller G, Lechner LG, Kusterer J, Kaiser U, Krill CE, Kohn E, Scholz F (2011) Graphene-based sample supports for in situ high-resolution TEM electrical investigations. *J Phys D Appl Phys* 44(5):055502. <https://doi.org/10.1088/0022-3727/44/5/055502>
47. Grogan JM, Rotkina L, Bau HH (2011) In situ liquid-cell electron microscopy of colloid aggregation and growth dynamics. *Phys Rev E* 83(6):061405. <https://doi.org/10.1103/PhysRevE.83.061405>
48. van Huis MA, Young NP, Pandraud G, Creemer JF, Vanmaekelbergh D, Kirkland AI, Zandbergen HW (2009) Atomic imaging of phase transitions and morphology transformations in nanocrystals. *Adv Mater* 21(48):4992–4995. <https://doi.org/10.1002/adma.200902561>
49. Allard LF, Bigelow WC, Jose-Yacamán M, Nackashi DP, Damiano J, Mick SE (2009) A new MEMS-based system for ultra-high-resolution imaging at elevated temperatures. *Microsc Res Tech* 72(3):208–215. <https://doi.org/10.1002/jemt.20673>
50. Chen X, Li C, Grätzel M, Kostecki R, Mao SS (2012) Nanomaterials for renewable energy production and storage. *Chem Soc Rev* 41(23):7909–7937. <https://doi.org/10.1039/c2cs35230c>
51. Yoshida K, Yamasaki J, Tanaka N (2004) In situ high-resolution transmission electron microscopy observation of photodecomposition process of poly-hydrocarbons on catalytic TiO<sub>2</sub> films. *Appl Phys Lett* 84(14):2542–2544. <https://doi.org/10.1063/1.1689747>
52. Yoshida K, Nanbara T, Yamasaki J, Tanaka N (2006) Oxygen release and structural changes in TiO<sub>2</sub> films during photocatalytic oxidation. *J Appl Phys* 99(8):084908. <https://doi.org/10.1063/1.2190721>
53. Zhang L, Miller B, Crozier P (2012) In situ analysis of TiO<sub>2</sub> photocatalysts under light exposure in the environmental TEM. *Microsc Microanal* 18(S2):1126–1127. <https://doi.org/10.1017/S1431927612007489>
54. Zhang L, Miller B, Crozier P (2012) CdS sensitized TiO<sub>2</sub> nanorod photocatalysts under light exposure in the environmental TEM. *Microsc Microanal* 18(S2):1298–1299. <https://doi.org/10.1017/S1431927612008343>
55. Yoshida K, Nozaki T, Tanaka N (2007) In-situ high-resolution transmission electron microscopy of liquid phase photocatalytic reaction that uses excited electrons by ionic liquid. *Microsc Microanal* 13(S02):982–983. <https://doi.org/10.1017/S1431927607072534>
56. Cavalca F, Laursen AB, Wagner JB, Damsgaard CD, Chorkendorff I, Hansen TW (2013) Light-induced reduction of cuprous oxide in an environmental transmission electron microscope. *ChemCatChem* 5(9):2667–2672. <https://doi.org/10.1002/cctc.201200887>
57. Griffiths JT, Zhang S, Rouet-Leduc B, Fu WY, Bao A, Zhu D, Wallis DJ, Howkins A, Boyd I, Stowe D, Kappers MJ, Humphreys CJ, Oliver RA (2015) Nanocathodoluminescence reveals mitigation of the Stark shift in InGaN quantum wells by Si doping. *Nano Lett* 15(11):7639–7643. <https://doi.org/10.1021/acs.nanolett.5b03531>
58. White ER, Howkins A, Williams CK, Shaffer MS (2015) Investigating the origin of luminescence in zinc oxide nanostructures with STEM-cathodoluminescence. *Microsc Microanal* 21(S3):1257–1258. <https://doi.org/10.1017/S1431927615007072>
59. Yang S, Tian X, Wang L, Wei J, Qi K, Li X, Xu Z, Wang W, Zhao J, Bai X, Wang E (2014) In-situ optical transmission electron microscope study of exciton phonon replicas in ZnO nanowires by cathodoluminescence. *Appl Phys Lett* 105(7):071901. <https://doi.org/10.1063/1.4893444>
60. Lim SK, Brewster M, Qian F, Li Y, Lieber CM, Gradečák S (2009) Direct correlation between structural and optical properties of III–V nitride nanowire heterostructures with nanoscale resolution. *Nano Lett* 9(11):3940–3944. <https://doi.org/10.1021/nl9025743>

61. Losquin A, Zagonel LF, Myroshnychenko V, Rodríguez-González B, Tencé M, Scarabelli L, Förstner J, Liz-Marzán LM, García de Abajo FJ, Stéphan O, Kociak M (2015) Unveiling nanometer scale extinction and scattering phenomena through combined electron energy loss spectroscopy and cathodoluminescence measurements. *Nano Lett* 15(2):1229–1237. <https://doi.org/10.1021/nl5043775>
62. Ringe E, DeSantis CJ, Collins SM, Duchamp M, Dunin-Borkowski RE, Skrabalak SE, Midgley PA (2015) Resonances of nanoparticles with poor plasmonic metal tips. *Sci Rep* 5(1):17431. <https://doi.org/10.1038/srep17431>
63. Zhao M, Bosman M, Danesh M, Zeng M, Song P, Darma Y, Rusydi A, Lin H, Qiu C-W, Loh KP (2015) Visible surface plasmon modes in single Bi<sub>2</sub>Te<sub>3</sub> nanoplate. *Nano Lett* 15(12):8331–8335. <https://doi.org/10.1021/acs.nanolett.5b03966>
64. Williams RE, Carnevale SD, Kent TF, Stowe DJ, Myers RC, McComb DW (2014) Electron energy loss spectroscopy and localized cathodoluminescence characterization of GaN quantum discs. *Microsc Microanal* 20(S3):578–579. <https://doi.org/10.1017/S1431927614004619>
65. Fern GR, Silver J, Coe-Sullivan S (2015) Cathodoluminescence and electron microscopy of red quantum dots used for display applications. *J Soc Inform Display* 23(2):50–55. <https://doi.org/10.1002/jsid.278>
66. Sutter P, Wimer S, Sutter E (2019) Chiral twisted van der Waals nanowires. *Nature* 570(7761):354–357. <https://doi.org/10.1038/s41586-019-1147-x>
67. den Engelsen D, Harris PG, Ireland TG, Fern G, Silver J (2015) Symmetry-related transitions in the photoluminescence and cathodoluminescence spectra of nanosized cubic Y<sub>2</sub>O<sub>3</sub>:Tb<sup>3+</sup>. *ECS J Solid State Sci Technol* 4(12):R145–R152. <https://doi.org/10.1149/2.0011512jss>
68. Kumar S, Nehra M, Deep A, Kedia D, Dilbaghi N, Kim K-H (2017) Quantum-sized nanomaterials for solar cell applications. *Renew Sustain Energy Rev* 73:821–839. <https://doi.org/10.1016/j.rser.2017.01.172>
69. Zhu L, Wang ZL (2019) Recent progress in Piezo-phototronic effect enhanced solar cells. *Adv Func Mater* 29(41):1808214. <https://doi.org/10.1002/adfm.201808214>
70. Wang X, Tian W, Liao M, Bando Y, Golberg D (2014) Recent advances in solution-processed inorganic nanofilm photodetectors. *Chem Soc Rev* 43(5):1400–1422. <https://doi.org/10.1039/c3cs60348b>
71. Yang T, Zheng Y, Du Z, Liu W, Yang Z, Gao F, Wang L, Chou K-C, Hou X, Yang W (2018) Superior photodetectors based on all-inorganic perovskite CsPbI<sub>3</sub> nanorods with ultrafast response and high stability. *ACS Nano* 12(2):1611–1617. <https://doi.org/10.1021/acsnano.7b08201>
72. Duan X, Huang Y, Cui Y, Wang J, Lieber CM (2001) Indium phosphide nanowires as building blocks for nanoscale electronic and optoelectronic devices. *Nature* 409(6816):66–69. <https://doi.org/10.1038/35051047>
73. Ide Y, Liu F, Zhang J, Kawamoto N, Komaguchi K, Bando Y, Golberg D (2014) Hybridization of Au nanoparticle-loaded TiO<sub>2</sub> with BN nanosheets for efficient solar-driven photocatalysis. *J Mater Chem A* 2(12):4150–4156. <https://doi.org/10.1039/c3ta13769d>
74. Li H, Wang X, Xu J, Zhang Q, Bando Y, Golberg D, Ma Y, Zhai T (2013) One-dimensional CdS nanostructures: a promising candidate for optoelectronics. *Adv Mater* 25(22):3017–3037. <https://doi.org/10.1002/adma.201300244>
75. Wang W, Zhao Q, Laurent K, Leprince-Wang Y, Liao Z-M, Yu D (2012) Nanorainforest solar cells based on multi-junction hierarchical p-Si/n-CdS/n-ZnO nanoheterostructures. *Nanoscale* 4(1):261–268. <https://doi.org/10.1039/c1nr11123j>
76. Yang H, Zhou Y, Yang Y, Yi D, Ye T, Lam TD, Golberg D, Bao B, Yao J, Wang X (2018) Crystal facet engineering induced anisotropic transport of charge carriers in a perovskite. *J Mater Chem C* 6(43):11707–11713. <https://doi.org/10.1039/c8tc04961k>
77. Zhang C, Cretu O, Kvashnin DG, Kawamoto N, Mitome M, Wang X, Bando Y, Sorokin PB, Golberg D (2016) Statistically analyzed photoresponse of elastically bent CdS nanowires probed by light-compatible in situ high-resolution TEM. *Nano Lett* 16(10):6008–6013. <https://doi.org/10.1021/acs.nanolett.6b01614>
78. Zhang C, Tian W, Xu Z, Wang X, Liu J, Li S-L, Tang D-M, Liu D, Liao M, Bando Y, Golberg D (2014) Photosensing performance of branched CdS/ZnO heterostructures as revealed by

- in situ TEM and photodetector tests. *Nanoscale* 6(14):8084–8090. <https://doi.org/10.1039/c4nr00963k>
79. Han X, Wang L, Yue Y, Zhang Z (2015) In situ atomic scale mechanical microscopy discovering the atomistic mechanisms of plasticity in nano-single crystals and grain rotation in polycrystalline metals. *Ultramicroscopy* 151:94–100. <https://doi.org/10.1016/j.ultramic.2014.11.035>
  80. Zhu Y, Milas M, Han M-G, Rameau J, Sfeir M (2012) Multimodal optical nanoprobe for advanced in-situ electron microscopy. *Microscopy Today* 20(6):32–37. <https://doi.org/10.1017/S1551929512000892>
  81. Ophus C (2019) Four-dimensional scanning transmission electron microscopy (4D-STEM): from scanning nanodiffraction to ptychography and beyond. *Microsc Microanal* 25(3):563–582. <https://doi.org/10.1017/S1431927619000497>
  82. Toyao T, Saito M, Dohshi S, Mochizuki K, Iwata M, Higashimura H, Horiuchi Y, Matsuoka M (2014) Development of a Ru complex-incorporated MOF photocatalyst for hydrogen production under visible-light irradiation. *Chem Commun* 50(51):6779–6781. <https://doi.org/10.1039/c4cc02397h>
  83. Toyao T, Ueno N, Miyahara K, Matsui Y, Kim T-H, Horiuchi Y, Ikeda H, Matsuoka M (2015) Visible-light, photoredox catalyzed, oxidative hydroxylation of arylboronic acids using a metal–organic framework containing tetrakis (carboxyphenyl) porphyrin groups. *Chem Commun* 51(89):16103–16106. <https://doi.org/10.1039/C5CC06163F>
  84. Shi E, Yuan B, Shiring SB, Gao Y, Akriti GY, Su C, Lai M, Yang P, Kong J, Savoie BM, Yu Y, Dou L (2020) Two-dimensional halide perovskite lateral epitaxial heterostructures. *Nature* 580(7805):614–620. <https://doi.org/10.1038/s41586-020-2219-7>
  85. Kwon O-H, Zewail AH (2010) 4D electron tomography. *Science* 328(5986):1668–1673. <https://doi.org/10.1126/science.1190470>
  86. Wang P, Zhang F, Gao S, Zhang M, Kirkland AI (2017) Electron ptychographic diffractive imaging of boron atoms in LaB6 crystals. *Sci Rep* 7(1):2857. <https://doi.org/10.1038/s41598-017-02778-x>
  87. Song B, Ding Z, Allen CS, Sawada H, Zhang F, Pan X, Warner J, Kirkland AI, Wang P (2018) Hollow electron ptychographic diffractive imaging. *Phys Rev Lett* 121(14):146101. <https://doi.org/10.1103/PhysRevLett.121.146101>